Heterobimetallic [NiFe] complexes containing mixed CO/CN^- ligands: analogs of the active site of the [NiFe] hydrogenases.

Carlo U. Perotto,[a] Charlene L. Sodipo,[a] Graham J. Jones,[a] Jeremiah P. Tidey,[a] Alexander J. Blake,[a] William Lewis,[a] E. Stephen Davies,[a] Jonathan McMaster,[a] and Martin Schröder*,[b]*

[a]School of Chemistry, University of Nottingham, Nottingham, NG7 2RD, U.K.

[b]The University of Manchester, Oxford Road, Manchester, M13 9PL, UK.

Abstract

The development of synthetic analogs of the active sites of [NiFe] hydrogenases remains challenging and, in spite of the number of complexes featuring a [NiFe] center, those featuring CO and CN^- ligands at the Fe center are under-represented. We report herein the synthesis of three bimetallic [NiFe] complexes [Ni(N_2S_2)Fe$(CO)_2(CN)_2$], [Ni(S_4)Fe$(CO)_2(CN)_2$] and [Ni(N_2S_3)Fe$(CO)_2(CN)_2$] that each contain a Ni center that bridges through two thiolato S donors to a {Fe$(CO)_2(CN)_2$} unit. X-ray crystallographic studies on [Ni(N_2S_3)Fe$(CO)_2(CN)_2$], supported by DFT calculations, are consistent with a solid state structure containing distinct molecules in the singlet (S = 0) and triplet (S = 1) states. Each cluster exhibits irreversible reduction processes between −1.45 to −1.67 V *vs* Fc^+/Fc and [Ni(N_2S_3)Fe$(CO)_2(CN)_2$] possesses a reversible oxidation process at 0.17 V *vs* Fc^+/Fc. Spectroelectrochemical infrared (IR) and electron paramagnetic resonance (EPR) studies, supported by density functional theory (DFT) calculations, are consistent with a $Ni^{III}Fe^{II}$ formulation for [Ni(N_2S_3)Fe$(CO)_2(CN)_2]^+$. The SOMO in [Ni(N_2S_3)Fe$(CO)_2(CN)_2]^+$ is based on Ni $3d_{z^2}$ and 3*p* S with the S contributions deriving principally from the apical S-donor. The nature of the SOMO corresponds to that proposed for the Ni-C state of the [NiFe] hydrogenases for which a $Ni^{III}Fe^{II}$ formulation has also been proposed. A comparison of the experimental structures, and the electrochemical and spectroscopic properties of [Ni(N_2S_3)Fe$(CO)_2(CN)_2$] and its [Ni(N_2S_3)] precursor, together with calculations on the oxidized [Ni(N_2S_3)Fe$(CO)_2(CN)_2]^+$ and [Ni(N_2S_3)]$^+$ forms suggests that the binding of the {Fe$(CO)(CN)_2$} unit to the {Ni$(CysS)_4$} center at the active site of the [NiFe] hydrogenases suppresses thiolate-based oxidative chemistry involving the bridging thiolate S donors. This is in addition to the role of the Fe center in modulating the redox potential and geometry, and supporting a bridging hydride species between the Ni and Fe centers in the Ni-C state.

Introduction

The [NiFe] hydrogenases catalyze the two-electron inter-conversion of two protons and molecular H_2, reactions that are relevant for the development of new clean energy technologies.[1] The active site of the [NiFe] hydrogenases consists of a heterobimetallic Ni-Fe cluster in which the Ni center is bound by two terminal cysteine S-donors and two cysteine S-donors that bridge to an Fe center that is also co-ordinated by one carbonyl and two cyanato ligands. Depending on the state of the enzyme, a third bridging ligand, X (X = OH^- or H^-), may also be found at the active site. In these states, the geometry about the Fe center is pseudo-octahedral and that about the Ni center is distorted square-based pyramidal, with X occupying a basal position. At least ten different states of the enzyme have been identified with formulations dependent on the oxidation state of the Ni center (*i*.e., Ni^{III}, Ni^{II} and Ni^{I}) and on the nature of X.[1c,1d,2] The importance of each state in the catalytic cycle continues to be debated,[1c,1d,3] but it is widely accepted that catalytic turnover is associated with changes of the formal oxidation state of the Ni center while the Fe center remains as low spin d^6 Fe^{II}.[2] The mechanisms proposed for catalysis[1c,1d,4] involve three key states, Ni-SI, Ni-R and Ni-C (Scheme 1) that involve the formal Ni^{II} (Ni-SI and Ni-R) and Ni^{III} oxidation states.[1c] Recent studies have also demonstrated the formation of the formal Ni^{I} Ni-L state in the dark under turnover conditions that may represent an intermediate in the regeneration of Ni-SI from Ni-C in the catalytic cycle.[5]

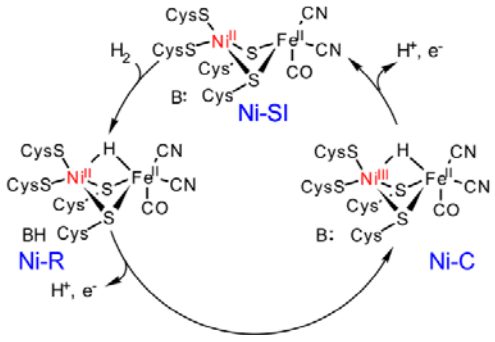

Scheme 1: A proposed catalytic cycle for H_2 oxidation by the [NiFe] hydrogenases.[1c,1d]

A range of analogs of the active site of the [NiFe] hydrogenases has been synthesized and characterized in attempts to replicate the principal structural and functional features of the active sites.[3,6] Complexes that possess a mixed CN^- and CO co-ordination about the Fe center, such as [Fe(*fac*-$CO)_3(CN)_3]^-$,[7] and Ni complexes that possess a $Ni^{III/II}$ couple with a relatively low reduction potential, such as $[Ni(ema)]^{2-}$ [ema^{4-} = *N*,*N*'-ethylenebis(2-(acetylthio)acetamide][8] have been reported. The development of structural, spectroscopic and functional analogs of the active sites of the [NiFe] hydrogenases has been challenging. In spite of a number of complexes featuring a [NiFe] center, relatively few compounds that possess the relevant ligation around the metal atoms have been reported. In particular, complexes featuring CO and CN^- ligands at the Fe center are under-represented with $(PPh_4)[(R_2NCS_2)Ni(pdt)Fe(CO)_2(CN)_2]$ (H_2pdt = 1,3-propanedithiol; R = Et- ; R_2 = $-(CH_2)_5-$), $(PPh_4)[(Et_2NCS_2)Ni(tpdt)Fe(CO)_2(CN)_2]$ (H_2tpdt = 3-thiapentanedithiol), and [(dxpe)Ni(pdt)Fe$(CO)_2(CN)_2$] [dxpe = 1,2-bis(diphenylphosphino)ethane (dppe), 1,2-bis(dicyclohexylphosphino)ethane (dcpe)] being the only examples.[9] H_2 reactivity and electrochemical studies have been limited to derivatives of [(dxpe)Ni(pdt)Fe$(CO)_2(CN)_2$], where the basicity of the CN^- ligands is moderated through interactions with $B(C_6F_5)_3$ to form [(dxpe)Ni(pdt)Fe$(CO)_2$(CN-$B(C_6F_5)_3)_2$]. In these complexes the redox events are associated principally with the Fe center rather than the Ni unit.[9c] There has been considerable success in reproducing key aspects of the proposed catalytic cycle for the [NiFe] hydrogenases and in the development of complexes containing a $[Ni^{II}Fe^{II}]$ center.[6e,10] However, the syntheses of relevant paramagnetic analogs have proven more challenging. $[Ni^{I}Fe^{II}]$[11] and $[Ni^{I}Ru^{II}]$[12] species that reproduce the electronic configuration of the Ni-center in the Ni-L state have emerged. In contrast, complexes possessing a $[Ni^{III}Fe^{II}]$ electronic configuration, characteristic of the Ni-C state,[1c] have proven more difficult to realize.

Herein we describe the syntheses, structures, and electrochemical and spectroscopic studies of the novel bimetallic [NiFe] complexes **1** – **3** (Scheme 2) featuring Ni centers incorporating polydentate ligands containing thiolato donors bound to a $Fe(CN)_2(CO)_2$ fragment. We also show that **3** undergoes reversible oxidation to yield a formal $[Ni^{III}Fe^{II}]$ complex that is reminiscent of the electronic structure of the $[Ni^{III}Fe^{II}]$ center proposed for the Ni-C state of the [NiFe] hydrogenases.

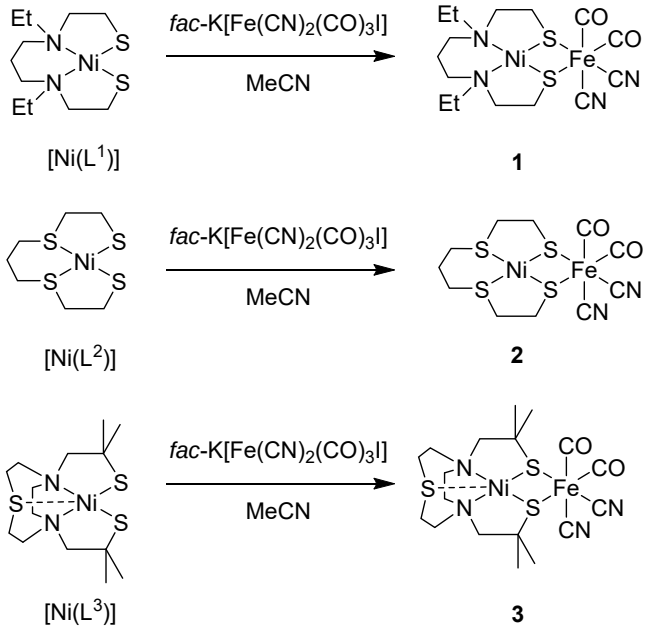

Scheme 2: Synthetic scheme for the syntheses of **1** – **3** from $[Ni(L^X)]$ (X = 1, 2, 3).

Experimental Section

General experimental procedures. Elemental analyses were carried out by the London Metropolitan University (Carlo Erba CE1108 Elemental Analyser). Infrared spectra were recorded on a Nicolet Avatar 360 FTIR spectrometer and solution infrared spectra were recorded using sealed solution cells with either CaF_2 or KBr windows. NMR spectra were recorded on Bruker DPX300, DPX400 or AV400 spectrometers. Mass spectra (ESI) were recorded by the Mass Spectrometry Service at the University of Nottingham. Electrochemical measurements were made using an Eco Chemie Autolab PGSTAT20

potentiostat. All solutions were purged with a stream of Ar prior to use. Cyclic voltammograms were performed using a three-electrode system with a glassy carbon working electrode (6.7 mm diameter), a Pt wire secondary electrode and a saturated calomel reference electrode. All potentials are referenced to the Fc^+/Fc couple that was used as an internal standard. Cyclic voltammograms were recorded for solutions of compound (*ca.* 1 mM) in MeCN with $[N^nBu_4][BF_4]$ (0.2 M) as the supporting electrolyte. Coulometric measurements were performed using an H-cell at 273 K in MeCN containing $[N^nBu_4][BF_4]$ (0.2 M); the cell consisted of a Pt/Rh gauze basket working electrode separated by a glass frit from a Pt/Rh gauze secondary electrode. The saturated calomel reference electrode was placed at the center of the working electrode and the solution stirred rapidly during electrolysis using a magnetic stirring bar. UV/vis spectroelectrochemical experiments were carried out at 273 K or 243 K using an optically transparent electrode mounted in a modified quartz cuvette with an optical pathlength of 0.5 mm. A three-electrode configuration consisting of a Pt/Rh gauze working electrode, a Pt wire secondary electrode (in a fritted PTFE sleeve) and a saturated calomel electrode, chemically isolated from the test solution *via* a bridge tube containing electrolyte solution and terminated in a porous frit, was used in the cell. The potential at the working electrode was controlled by a Sycopel Scientific Ltd. DD10M potentiostat. UV/vis spectra were recorded on a Perkin Elmer Lambda 16 spectrophotometer. The spectrometer cavity was purged with N_2 and temperature control at the sample was achieved by flowing cooled N_2 across the surface of the cell. X-band EPR spectra were recorded on a Bruker EMX spectrometer. The simulations of the EPR spectra were performed using the Bruker WINEPR SimFonia package.

X-ray crystallography. Crystals of **1**A and **1**B were collected on a Bruker SMART APEX diffractometer with graphite-monochromated Mo$K\alpha$ radiation (λ = 0.71073 Å). Crystal of **2** and **3** were

examined on a Rigaku Oxford Diffraction SuperNova diffractometer using mirror-monochromated Cu$K\alpha$ radiation (λ = 1.5418 Å). Intensities were integrated from data recorded on 0.3° (**1**A and **1**B) or 1° (**2** and **3**) frames by ω rotation. Cell parameters were refined from the observed positions of all strong reflections in each data set. Either a multiscan absorption correction[13] (**1**A and **1**B) or Gaussian grid face-indexed absorption correction with a beam profile correction[14] (**2** and **3**) was applied. The structures were solved by direct (**1**A, **1**B and **2**)[15] or charge flipping[16] (**3**) methods and were refined by full-matrix least-squares on all unique F^2 values.[17] Anisotropic displacement parameters were refined for all non-hydrogen atoms; hydrogen atoms were geometrically constrained with U_{iso}(H) set at 1.2 (1.5 for methyl groups) times U_{eq} of the parent atom. During the structure analysis, the crystal of **1**A was discovered to be a pseudo-merohedral twin. The TWINROTMAT routine in PLATON[18] was used to deconvolute the twin components and produce a file suitable for subsequent twin refinement. There are two possible orientations for the carbon atoms of the S_2N_2 ligand. The occupancies of the two components were refined competitively, converging at a ratio of 0.67:0.33. The lengths of chemically equivalent bonds of the disordered atoms were restrained to be approximately equal. Enhanced rigid bond and similarity restraints[17] were applied to the displacement parameters of all non-hydrogen atoms.

Computational details. All DFT calculations were performed using Gaussian 03.[19] Geometry optimizations and IR spectra were calculated using the BP86 functional.[20] Single point electronic calculations were performed using the three-parameter hybrid exchange functional[21] and the Lee-Yang-Parr correlation function[22] (B3LYP). For geometry optimizations, the basis set was an adapted version of that used by Hall *et al.*.[23] The Ni and Fe atoms were described by the Hay and Wadt basis set[24] with an effective core potential (ECP); the 4p orbitals in the ECP basis set were replaced by optimized (41) split valence functions from Couty and Hall[25] and augmented by an f-polarization function.[26] The standard

LANL2DZ basis set was augmented with a d-polarization and p-diffuse function for S.[27] The 6-31G(d,p)[28] basis set was used for the H, C and N atoms of the polydentate ligands about the Ni centers and the C, N and O atoms of the CO and CN^- were described by the 6-311G(d,p) basis set. After each optimization a frequency analysis was performed to confirm that the stationary point was found to be a minimum on the potential energy surface. For electronic properties the all-electron Wachters (+f) basis set was used for Ni and Fe while the C, H, S and N atoms were described with the 6-311G(d,p) basis set.[29] Unrestricted calculations of the spin Hamiltonian parameters for $[Ni(L^3)]^+$ and $[\mathbf{3}]^+$ used the B3LYP and PBE0 functionals, the all-electron Wachters (+f) basis set for Ni and Fe, the EPRII basis set for the C, H and N atoms and the 6-311G(d,p) basis set for S.[29-30] Visualization of the structures and isosurface plots of electronic properties were obtained with the program Molekel (version 5.4.0.8)[31] and NAO analyses were carried out using the programs Multiwfn[32] and NBO 3.1.[33] Multiwfn[32] was used to prepare plots of the calculated IR spectra of **1** and **2**. Models of **1** and **2** (S = 0, *cis*-CN_{endo}, *cis*-CO_{endo}, *trans*-CN, and *trans*-CO isomers, see Supplementary Information), $[Ni(L^3)]$ (S = 0, 1), $[Ni(L^3)]^{3+}$, **3** (S = 0, 1) and $[\mathbf{3}]^+$ were constructed using the geometrical data from the X-ray crystal structures of $[Ni(L^3)]$ and **3**. The co-ordinate frame employed in the calculations of $[Ni(L^3)]$ (S = 0, 1), $[Ni(L^3)]^{3+}$, **3** (S = 0, 1) and $[\mathbf{3}]^+$ is shown in Figure 7. The *x* axis bisects the S(1)-Ni(1)-S(2) angle and the *y* axis lies in the plane defined by S(1)-Ni(1)-S(2).

Synthesis and materials. All reactions and manipulations were carried out under an Ar atmosphere using standard Schlenk techniques. Unless otherwise stated, the reagents were used as received from the suppliers (Sigma-Aldrich, Acros Organic and Fluka). $[Ni(L^1)]$, $[Ni(L^2)]$, $[Ni(L^3)]$ and *fac*-$K[Fe(CN)_2(CO)_3I]$ were prepared according to literature procedures.[9a,34] Solvents were dried and

degassed following standard procedures and stored under Ar in Young's ampoules over molecular sieves (pore size 4 Å).

The synthesis of [Ni(L^1)Fe(CO)$_2$(CN)$_2$] (1): A solution of [Ni(L^1)] (100 mg, 0.32 mmol) in MeCN (5 mL) was added dropwise to a solution of *fac*-K[Fe(CN)$_2$(CO)$_3$I] (115 mg, 0.32 mmol) in MeCN (10 mL) in the absence of light. The reaction mixture turned from pale orange to deep red as the addition proceeded. After stirring for 1.5 h the solution was filtered and the solvent was removed under vacuum. The red solid obtained was extracted with CH_2Cl_2 (10 mL), and the solution filtered and evaporated to dryness under vacuum. Extraction with THF (6 × 8 mL) followed by removal of the solvents under reduced pressure afforded **1** as an orange-red solid (50 mg, 48 %). ESI-MS (*m*/*z*): $[M+HCOO]^-$ calcd for $C_{16}H_{25}FeN_4NiO_4S_2$, 515.0020; found 515.0015; $[M+Cl]^-$ calcd for $C_{15}H_{24}FeN_4NiO_2S_2Cl$, 515.9747; found 504.9727. The complex is a mixture of two isomers, *trans*-CN (**1**A) and *cis*-CN_{endo} (**1**B), that can be separated on an alumina (grade 3) column using CH_2Cl_2/MeOH (1 % v/v) as eluent. The first band isolated contains **1**A. The second band requires elution with CH_2Cl_2/MeOH (8 % v/v). **1**A: FTIR (MeCN) ν_{CN} (cm^{-1}) 2117 (w), 2101 (w); ν_{CO} (cm^{-1}) 2049 (s), 1999 (s). ^{1}H NMR (400 MHz, CD_2Cl_2) δ ppm 1.49 (t, J = 7.12 Hz, NCH_2CH_3 , 6 H) 1.74 (m, 2 H) 2.07 - 2.26 (m, 2 H) 2.29 - 2.50 (m, 2 H) 2.59 - 2.80 (m, 6 H) 3.10 (m, 2 H) 3.30 - 3.46 (m, 2 H) 3.54 (m, 2 H). **1**B: FTIR (MeCN) ν_{CN} (cm^{-1}) 2115 (w); ν_{CO} (cm^{-1}) 2047 (s), 1999 (s). ^{1}H NMR (400 MHz, CD_3CN) δ ppm 1.29 (t, J = 6.92 Hz, 3 H, NCH_2CH_3) 1.34 (t, J = 6.92 Hz, 3 H, NCH_2CH_3) 1.74 (m, 1 H) 2.09 (m, 2 H) 2.41 (m, 3 H) 2.60 (br. s., 2 H) 2.73 (m, 2 H) 2.83 - 3.05 (m, 2 H) 3.15 (m , 4 H) 3.54 (m, 1 H) 3.79 (m, 1 H). Single crystals of each isomer were grown by layering Et_2O anti-solvent over a solution of the complex in MeCN.

The synthesis of [Ni(L^2)Fe(CO)$_2$(CN)$_2$] (2): A solution of *fac*-K[Fe(CN)$_2$(CO)$_3$I] (150 mg, 0.4 mmol) in MeCN (10 mL) was added dropwise to a suspension of [Ni(L^2)] (100 mg, 0.35 mmol) in MeCN (5

mL) in the dark. The reaction mixture turned from red to orange. After stirring for 12 h the solution was filtered and the solvent removed under vacuum. The red solid was extracted with CH_2Cl_2 (3 × 10 mL) and the solution filtered and evaporated to dryness to afford **2** as an orange-red microcrystalline solid (50 mg, 11 %). ESI-MS (*m*/*z*): $[M+Na]^+$ calcd for $C_{11}H_{14}FeN_2NaNiO_2S_4$, 470.8538; found 470.8539. Anal. Calcd. for $C_{11}H_{14}FeN_2NiO_2S_4$: C, 29.42; H, 3.14; N, 6.24 %. Found C, 29.40; H, 3.02; N, 6.10 %. The complex is a mixture of two isomers that can be separated on an alumina (grade 3) column using CH_2Cl_2/MeCN (50 % v/v) as eluent. The first band isolated contains the *trans*-CN isomer (**2**A) but the second band could be only partially recovered and insufficient quantities of the *cis*-CN_{endo} isomer (**2**B) were obtained for characterization. **2**A: FTIR (MeCN) ν_{CN} (cm^{-1}) 2120 (w), 2101 (w); ν_{CO} (cm^{-1}) 2054 (s), 2005 (s). ^{1}H NMR (400 MHz, CD_3CN) δ ppm 1.71 (dtt, J = 16.20, 13.30, 2.50 Hz, 1 H, $SCH_2CH_2CH_2S$) 2.66 - 2.80 (m, 5 H, NC_2H_4S) 2.84 (ddd, J = 11.30, 5.40, 2.00 Hz, 2 H, $SCH_2CH_2CH_2S$) 2.88 (d, J = 5.41 Hz, 1 H, $SCH_2CH_2CH_2S$) 2.89 - 2.98 (m, 1 H, NC_2H_4S) 3.01 - 3.12 (m, 2 H, NC_2H_4S) 3.79 (ddd, J = 13.30, 11.40, 2.00 Hz, 2 H, $SCH_2CH_2CH_2S$). **2**B: FTIR (MeCN) ν_{CN} (cm^{-1}) 2117 (w); ν_{CO} (cm^{-1}) 2052 (s), 2005 (s).

The synthesis of $[Ni(L^3)Fe(CO)_2(CN)_2]$ (3): A solution of $[Ni(L^3)]$ (50 mg, 0.13 mmol) in MeCN (5 mL) was added dropwise to a solution of *fac*-$K[Fe(CN)_2(CO)_3I]$ (60 mg, 0.17 mmol) in MeCN (10 mL) in the absence of light. After stirring for 6 h an additional portion of *fac*-$K[Fe(CN)_2(CO)_3I]$ (20 mg, 0.06 mmol) was added to the reaction mixture and the mixture stirred for a further 3 h. The reaction mixture was filtered and the resulting solution was evaporated to dryness. The red solid was extracted with CH_2Cl_2 (3 × 10 mL), the solution was filtered and the removal of solvent under reduced pressure afforded **3** as an orange-red microcrystalline solid (10 mg, ~15%). Anal. Calcd for $C_{18}H_{28}FeN_4NiO_2S_3$: C, 39.82; H, 5.20; N, 10.32 %. Found: C, 40.26; H, 5.28; N, 10.67 %. ESI-MS (*m*/*z*): $[M+Na]^+$ calcd for

$C_{18}H_{28}FeN_4NiO_2S_3$, 564.9975; found 564.9937. FTIR (MeCN): ν_{CN} (cm^{-1}) 2117 (w), 2100 (w); ν_{CO} (cm^{-1}) 2044 (s), 1994 (s).

Results and Discussion

Synthetic approach. The synthetic schemes for the preparation of previous [NiFe] complexes incorporating CO and CN^- ligands about the Fe center involve the reaction of either *mer,trans*-$[Fe(CO)_3(CN)_2Br]^-$ or *fac,cis*-$[Fe(CO)_3(CN)_2I]^-$ with a dithiolate ligand, followed by the reaction of the resulting Fe-dithiolate complex with an appropriate Ni-precursor such as $Ni(dppe)Cl_2$ or $[Ni(PPh_3)Br(S_2CNR_2)]$.[9a,9b,35]

We adapted this approach and found that compound **1** (Scheme 2) can be readily synthesized by reaction of *fac*-$[Fe(CO)_3(CN)_2I]^-$[9a] with $[Ni(L^1)]$ in MeCN. The ^{1}H-NMR spectrum of **1** clearly indicates the presence of two isomers, revealed by resonances assigned to the methyl groups of the ethyl substituents pendant to the amine donors in **1** (Figure S1). Taking into account the butterfly shape, typical of the $Ni(\mu\text{-}S)_2Fe$ motif, four isomers are possible that differ in the arrangement of the CO and CN^- ligands about the Fe center (Scheme 3). A comparison with the isomerism reported for $[(dcpe)Ni(pdt)Fe(CO)_2(CN)_2]$ suggests that **1** is a mixture of the *trans*-CN and one of the two possible *cis*-CN/*cis*-CO isomers.[9c]

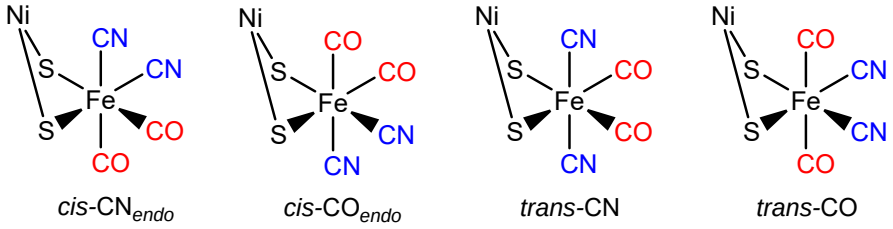

Scheme 3: View of the four possible isomers deriving from the arrangements of the CO and CN^- ligands about the Fe center.

The separation of the two isomers of **1** was achieved by column chromatography on alumina using CH_2Cl_2/MeCN as eluent. The assignment of the two isomers as *trans*-CN (**1**A) and the *cis*-CN_{endo} (**1**B) in solution is supported by X-ray crystallography (*vide infra*) and by DFT calculations (see Supplementary Information). The IR spectrum of **1**A in MeCN solution possess two ν_{CN} bands of equal intensity at 2117 and 2101 cm^{-1} and two ν_{CO} bands at 2049 and 1999 cm^{-1}, while that of **1**B exhibits two intense ν_{CO} bands at 2047 and 1999 cm^{-1} and one ν_{CN} band at 2115 cm^{-1} (Figure 1). The expected second ν_{CN} band for **1**B is not resolved in the experimental spectrum and DFT calculations of the *cis*-CN_{endo} suggest that the antisymmetric ν_{CN} stretch in **1**B is of relatively low intensity and/or may overlap with other bands (see Supplementary Information). The frequencies of the CO stretching vibrations are similar in **1**A and **1**B, consistent with the retention of the *cis*-CO configuration in both compounds. Considering that the syntheses start from the *cis*-CN complex, *fac*-$[Fe(CO)_3(CN)_2I]^-$, the formation of the *trans*-CN isomer must result from a ligand rearrangement during the reaction with $[Ni(L^1)]$.[9a] **1** is stable in aprotic solvents at room temperature in the dark as monitored by IR spectroscopy over a 6 h period, but is sensitive to light. The irradiation of a solution of **1** in MeCN with a white LED or exposure to direct sunlight for 20 sec leads to the complete loss of the ν_{CO} and ν_{CN} bands and the evolution of gas, presumably CO.

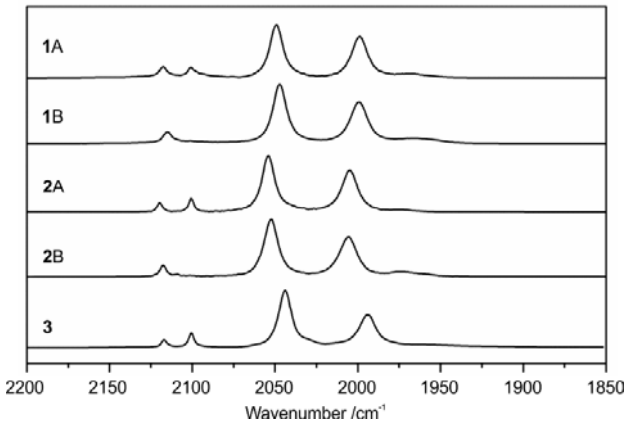

Figure 1: The IR spectra of **1 - 3** recorded in MeCN solution.

The synthetic method developed for the synthesis of **1** was extended to reactions involving [Ni(L^2)] [H_2L^2 = 1,4,8,11-tetrathiaundecane][34b] and [Ni(L^3)] [H_2L^3 = 4,7-bis(2'-methyl-2'-mercaptopropyl)-1-thia-4,7-diazacyclononane][34c] and *fac*-[$Fe(CO)_3(CN)_2I]^-$. The reactions of [Ni(L^2)] and [Ni(L^3)] with *fac*-K[$Fe(CO)_3(CN)_2I$] in MeCN are considerably slower than that for **1**, possibly because of the low solubility of [Ni(L^2)] in MeCN and the increased steric requirements for the *gem* methyl groups in α-positions to S in [Ni(L^3)]. **2** was obtained as a mixture of two isomers assigned to the *trans*-CN (**2**A) and *cis*-CN_{endo} (**2**B) forms in solution on the basis of their experimental and calculated IR spectra (Fig 2 and Supplementary Information). This assignment is supported by the solid state structure of **2**A and the assignments of the isomers of **1**. **3** was isolated as the *trans*-CN isomer (Scheme 2). The substitution chemistry of *fac*-K[$Fe(CO)_3(CN)_2I$] is complex and can lead to multiple products in solution.[36] Therefore in the synthesis of **3**, two additions to give an excess of *fac*-K[$Fe(CO)_3(CN)_2I$] were made to maximize the yield of **3**.

X-ray Crystallography of 1 - 3

The X-ray crystal structures of **1** – **3** are shown in Figure 2 and selected bond distances and angles are presented in Table 1.

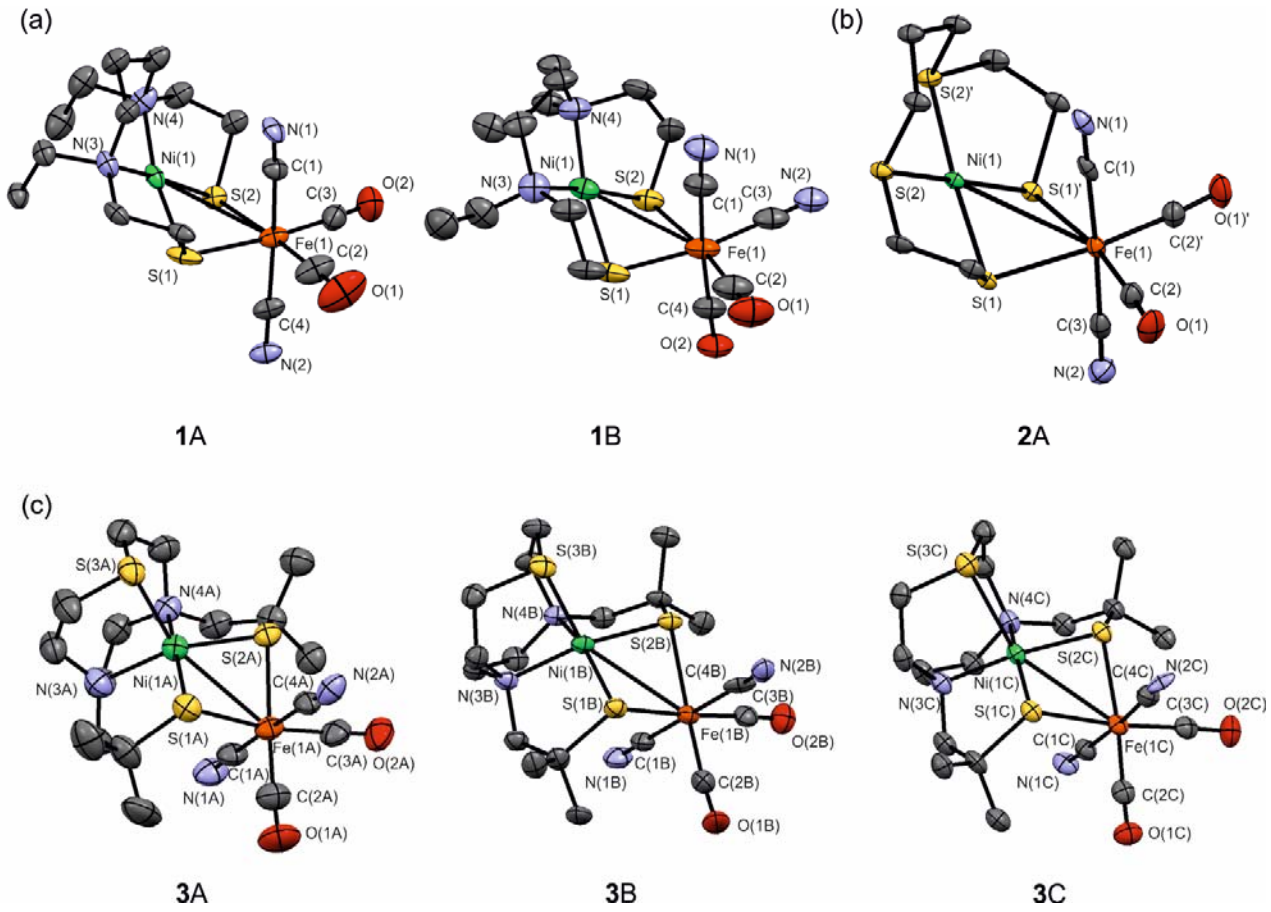

Figure 2: X-ray crystal structures of (a) **1** as the *trans*-CN (**1**A) and *cis*-CN$_{endo}$ (**1**B) isomers, (b) **2**A and (c) **3** as three independent molecules (**3**A, **3**B and **3**C) in the asymmetric unit. Displacement ellipsoids plotted at the 50% probability level and hydrogen atoms are omitted for clarity.

Table 1: Selected Bond Distances (/Å) and angles (/º) for the X-ray structures of **1 - 3** and gas-phase DFT geometry optimizations for models of $[\mathbf{3}]^{0/+}$.

	1A	**1**B	**2**A	**3**A	**3**B	DFT S = 1	**3**C	DFT S = 0	DFT $\mathbf{3}^{+}$
Ni(1)···Fe(1)	3.175(3)	3.1519(11)	3.0912(12)	3.0745(17)	3.1033(13)	2.914	3.0998(13)	3.114	2.973
Ni(1)-C(1)	3.056(13)	3.048(6)	2.923(5)	3.140(7)	3.207(6)	2.934	3.063(6)	3.030	2.903
Ni(1)-S(1)	2.184(4)	2.1649(13)	2.1750(9)	2.273(2)	2.2812(16)	2.319	2.1846(17)	2.221	2.241
Ni(1)-S(2)/S(1)'	2.172(3)	2.1645(13)	2.1750(9)	2.284(2)	2.2732(18)	2.327	2.1697(19)	2.205	2.230
Ni(1)-S(3)	-	-	-	2.362(2)	2.372(2)	2.350	2.6856(19)	2.753	2.395
Ni(1)-N(3)	2.007(10)	2.009(4)	-	2.077(7)	2.073(5)	2.166	1.967(5)	2.011	2.026
Ni(1)-N(4)	2.022(12)	2.003(4)	-	2.078(7)	2.071(5)	2.154	1.967(5)	2.003	2.028
S(1)-Ni(1)-S(2)/S(1)'	82.32(13)	81.79(5)	85.60(5)	90.65(8)	89.41(6)	97.0	87.57(6)	88.1	91.1
N(3)-Ni(1)-N(4)	98.8(4)	99.87(17)	-	86.1(3)	86.0(2)	84.5	88.9(2)	88.7	89.2
N(3)-Ni(1)-S(2) (α)	171.0(3)	169.23(13)	-	158.0(2)	165.93(16)	169.9	172.65(17)	174.0	175.5
N(3)-Ni(1)-S(1)	89.7(3)	88.79(13)	-	89.8(2)	88.73(14)	87.5	90.15(16)	90.4	88.9
N(4)-Ni(1)-S(2)	88.6(3)	89.03(13)	-	88.4(2)	89.93(16)	88.4	91.18(15)	91.2	89.7
N(4)-Ni(1)-S(1) (β)	168.6(3)	169.62(14)	-	166.6(2)	155.32(15)	180.3	162.90(16)	164.2	165.9
Fe(1)-S(1)	2.315(4)	2.3199(16)	2.3354(9)	2.389(2)	2.3873(18)	2.431	2.3667(17)	2.408	2.377
Fe(1)-S(2)/S(1)'	2.314(4)	2.3348(13)	2.3354(9)	2.378(2)	2.3594(16)	2.430	2.3548(16)	2.411	2.375
Fe(1)-C(1)	1.938(13)	1.955(5)	1.945(5)	1.938(8)	1.944(7)	1.919	1.941(6)	1.925	1.924
Fe(1)-C(2)	1.768(16)	1.790(6)	1.795(3)	1.789(9)	1.788(7)	1.753	1.790(7)	1.751	1.768
Fe(1)-C(3)/C(2)'	1.792(16)	1.912(6)	1.795(3)	1.788(9)	1.786(7)	1.753	1.792(7)	1.752	1.769
Fe(1)-C(4)/C(3)	1.939(13)	1.809(4)	1.953(5)	1.974(8)	2.052(8)	1.929	1.936(3)	1.929	1.927
S(1)-Fe(1)-S(2)/S(1)'	76.53(14)	75.02(5)	78.51(5)	85.65(7)	84.90(6)	91.45	79.31(6)	79.37	84.4
C(1)-Fe(1)-C(4)/C(3)	175.4(6)	175.9(2)	177.43(18)	179.2(3)	176.4(3)	174.2	176.8(3)	174.3	173.9
C(2)-Fe(1)-C(3)/C(2)'	92.7(8)	96.8(3)	98.1(2)	92.3(5)	92.3(3)	91.3	92.3(3)	91.3	88.9
Ni-S_2/Fe-S_2	133.4(2)	129.58(6)	130.37(4)	133.2(1)	134.10(8)	128.4	132.16(8)	129.3	126.8
τ [= (|α-β|)/60][37]				0.14	0.18	0.17	0.16	0.16	0.16

A common feature of the structures of **1 - 3** is that each Ni unit binds to the Fe center as a bidentate metallodithiolate ligand. The Fe center in each **1 - 3** possesses a distorted octahedral geometry while the Ni center adopts distorted square-planar co-ordination in **1** and **2**A, and a distorted square-based pyramidal geometry in **3**. Complexes **1 - 3** were structurally characterized as the *trans*-CN (**1**A), *cis*-CN_{endo} (**1**B), the *trans*-CN (**2**A) and *trans*-CN (**3**) isomers (Figure 2). The previously reported analogs $[(R_2NCS_2)Ni(pdt)Fe(CO)_2(CN)_2]^{2-}$ and $[(dppe)Ni(pdt)Fe(CO)_2(CN)_2]$ were characterized only as their *trans*-CN isomers in contrast to the *cis*-CN arrangement found at the Fe center at the active sites of the [NiFe] hydrogenases.[9a-c] The distinction between the CO and CN^- ligands in each structure is revealed by the Fe-CN and Fe-CO distances (Table 1, average 1.9 *versus* average 1.8 Å, respectively) reflecting the difference in π-acidity of the CO and CN^- ligands.[9b] The directionality of the lone pairs of electrons associated with the S(1) and S(2)/S(1)' atoms induces a butterfly shape for the $\{NiS_2Fe\}$ unit in **1 - 3** that brings one of the apical C donors from one of the CO or CN^- ligands into a potential bridging position between the Ni and Fe atoms. The Ni-C(1) distances for **1 - 3** vary from 3.207(6) Å for *trans*-CN in **3**B to 2.923(5) Å for *trans*-CN in **2**A. These values fall outside of the sum of the empirical atomic radii[38] for Ni and C (1.35 + 0.70 = 2.05 Å) that suggest there is little Ni(1)-C(1) interaction. This is supported by the IR spectra of **1** – **3** that show no bands that correspond to CO or CN^- ligands in a bridging position between the Ni and Fe centers (*vide infra*). The Ni(1)-Fe(1) distances range from 3.175(3) to 3.0745(17) Å (Table 1) and are *ca.* 0.2 Å greater than the Ni-Fe distances of the oxidized states of [NiFe] hydrogenases (*e.g.*, 2.92 Å for the Ni-A state of *D. fructosovorans*).[6g] The separation between the Ni and Fe centers also appears to show some correlation with the dihedral angle between the NiS_2 and FeS_2 planes (Table 1) that may be related to the steric requirements of the Ni moiety and intramolecular electronic interactions.[39]

The crystal lattice of **3** contains three independent molecules (**3**A, **3**B and **3**C) in the asymmetric unit. Molecules **3**A and **3**B possess similar geometries whereas **3**C displays a significant elongation of the apical Ni(1)-S(3) distance [2.6856(19) Å for **3**C *vs* 2.362(2) Å and 2.372(2) Å for **3**A and **3**B, respectively] and a contraction of the equatorial Ni(1)-S(1)/S(2) and Ni(1)-N(3)/N(4) distances [av. Ni(1)-S = 2.177 Å and Ni(1)-N = 1.967 Å for **3**C *vs* av. Ni(1)-S = 2.278 Å and Ni(1)-N = 2.075 Å for **3**A and **3**B]. These variations about Ni(1) are not translated to the geometry about the Fe center, which remains essentially invariant in **3**A, **3**B and **3**C. The geometry of the Ni units in **3**A and **3**B is consistent with a high-spin, square-based pyramidal Ni-center whereas **3**C is tetragonally distorted towards a geometry which resembles that of the [Ni(L^3)] precursor (Table 1). In the solid state structure of [Ni(L^3)] at 100 K, the Ni(1)-S(3) distance [2.8235(8) Å] suggests that [Ni(L^3)] approaches a low-spin, square-planar geometry under these conditions.[34c] Our gas-phase geometry optimized DFT calculations for **3** in the triplet (S = 1) state (*vide infra*) reveal geometric parameters that show a close correspondence to those for the experimental geometries of **3**A and **3**B. A gas-phase geometry optimization of a model of **3** in the singlet (S = 0) state reproduces the elongation of the axial Ni(1)-S(3) distance and the contraction of the equatorial bonds as observed experimentally for **3**C (Table 1). Thus, it appears that **3** displays a phase in the solid state where high-spin (**3**A and **3**B) and essentially low-spin (**3**C) species coexist.[40] Penta-co-ordinate Ni^{II} complexes can exhibit temperature-dependent spin crossover that may be accompanied by a significant elongation of the axial bond at the Ni center. For example, solid-state X-ray crystallographic and magnetic susceptibility measurements show two distinct molecules of [($Tp^{Ph,Me}$-)Ni(S_2CNMe_2)] [$Tp^{Ph,Me}$ = hydrotris(3-phenyl-5-methyl-1-pyrazolyl)borate] at 123 K, one in a S = 1 state and one in a S = 0 state with an elongated axial Ni(1)-N bond and contracted equatorial bonds.[41]

Electrochemical characterizations of 1 - 3

The electrochemical properties of **1 - 3** and of their precursors [Ni(L^1)], [Ni(L^2)] and [Ni(L^3)], respectively, were investigated by cyclic voltammetry in MeCN solution with 0.2 M [N^nBu_4][BF_4] as the supporting electrolyte (Figs. SI2-SI4, Figure 3 and Table 2). [Ni(L^1)], [Ni(L^2)] and [Ni(L^3)] undergo irreversible reduction at −2.40 to −2.02 V *vs* Fc^+/Fc and **1 - 3** undergo an irreversible reduction in the −1.45 to −1.67 V *vs* Fc^+/Fc potential range. The potentials for **1 - 3** are *ca.* 0.6 - 0.8 V more positive relative to those for [Ni(L^1)], [Ni(L^2)] and [Ni(L^3)], which is consistent with the presence of a {$Fe(CO)_2(CN)_2$} unit in **1 - 3** that withdraws electron density from the Ni fragment *via* the bridging thiolate S donors.[39] The potential of the reduction process becomes more anodic along the series **3** < **1** < **2** and mirrors that for the [Ni(L^X)] precursors where the potential for the reduction process also follows the trend [Ni(L^3)] < [Ni(L^1)] < [Ni(L^2)]. The differences in potential reflect substitution of thioether donors in [Ni(L^2)] with the stronger-field N donors in [Ni(L^1)], and the incorporation of an additional S donor in [Ni(L^3)]. This increase in electron density about the Ni center is also reflected in the IR spectra of **1 - 3** in the ν_{CO} stretching region (Table 3). The force constant calculated for each ν_{CO} follows the order **2** > **1** > **3**, consistent with a greater degree of Fe-CO backbonding as the electron density about the Ni center increases.

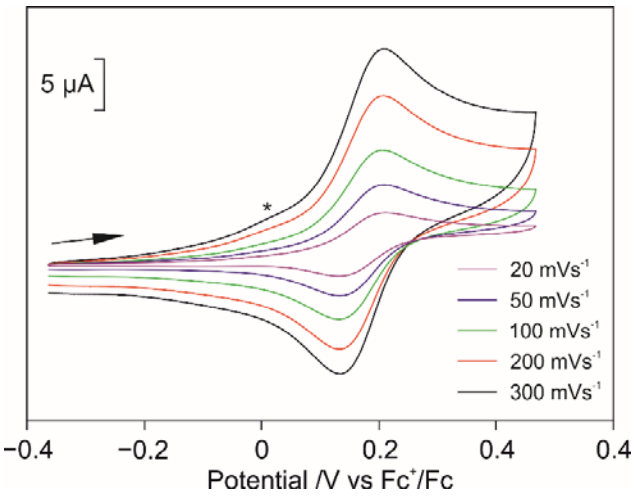

Figure 3: Cyclic voltammograms of a solution of **3** (1 mM) in MeCN with 0.2 M $[N^nBu_4][BF_4]$ as supporting electrolyte. *assigned to the presence of minor impurities due to the photodecomposition of the sample.

Table 2: The cathodic and anodic peak potentials, and oxidation potentials for solutions of $Ni(L^X)$ (X = 1, 2 and 3) and **1 - 3** (1 mM) in MeCN with 0.2M $[N^nBu_4][BF_4]$ as supporting electrolyte.

Complex	E_p^c first process /V *vs* Fc^+/Fc	E_p^a first process /V *vs* Fc^+/Fc	$E_{½}$ second process /V *vs* Fc^+/Fc
$Ni(L^1)$	−2.35	-	
$Ni(L^2)$	−2.02	-	
$Ni(L^3)$	−2.38	−2.28	−0.60
1	−1.57	−1.31	
2	−1.45	−1.37	
3	−1.67	-	0.17

Table 3: Infra red spectroscopic data for the ν_{CO} and ν_{CN} stretching regions and force constants for the CO stretches for complexes **1 - 3** recorded as solutions in MeCN.

Complex	ν_{CN} /cm^{-1}	ν_{CO} /cm^{-1}	k_1 /mdyn $Å^{-1}$	k_i /mdyn $Å^{-1}$
1A	2117, 2101	2049, 1999	16.55	0.41
1B	2115	2047, 1999		
2A	2120, 2101	2054, 2005	16.64	0.40
2B	2117	2052, 2005		
3	2117, 2100	2044, 1994	16.47	0.41

The variation in reduction potential for **1** - **3** with the nature of the co-ordination about the Ni center also suggests that the reduction process is associated with the Ni center *via* a $Ni^{II}Fe^{II}/Ni^{I}Fe^{II}$ couple. This is supported by DFT calculations that show the LUMO is localized at the NiN_2S_2, NiS_4 and NiN_2S_3 centers in **1** – **3**, respectively (see Supplementary Information). However, the chemically irreversible nature of this process precludes further study and a definitive assignment of the products of reduction cannot be confirmed. **3** also exhibits an oxidation process at 0.17 V *vs* Fc^+/Fc, which is electrochemically reversible over the 20 – 300 mVs^{-1} range of scan rates (Figure 3). A reversible oxidation process is also observed for [Ni(L^3)] at −0.60 V *vs* Fc^+/Fc that is assigned to the Ni^{III}/Ni^{II} couple (Figure S4) on the basis of the EPR spectroscopic results for [Ni(L^3)]$^+$ (*vide infra*). This, together with the EPR spectroscopic results for [**3**]$^+$, suggests that the [**3**]$^{+/0}$ redox process may also be largely Ni-based and may be assigned as a formal $Ni^{III}Fe^{II}/Ni^{II}Fe^{II}$ couple.

Spectroelectrochemistry of 3

[**3**]$^+$ was generated electrochemically by the controlled potential electrolysis of **3** in MeCN solution containing 0.2 M [N^nBu_4][BF_4] as supporting electrolyte at 253 K at a potential of 0.5 V *vs* Fc^+/Fc. The orange/red solution appeared to darken during the oxidation of **3** to [**3**]$^+$. The cyclic voltammograms of the solution recorded before and after the electrolysis experiment [Figure 4(a)] possess similar profiles, indicating that [**3**]$^+$ is stable over the timescale of the controlled potential electrolysis experiment.

The IR difference spectrum between [**3**]$^+$ and **3** shows that the CO and CN^- bands at 2117, 2100, 2043 and 1993 cm^{-1} of **3** deplete while new features at 2125, 2109, 2071 and 2033 cm^{-1} develop following the oxidation of **3** to [**3**]$^+$ in MeCN solution with 0.2 M [N^nBu_4][BF_4] as supporting electrolyte [Figure 4(b)]. The shift of each ν_{CO} and ν_{CN} band to higher frequencies in [**3**]$^+$ is consistent with a reduction of electron density about the Fe center and a consequent decrease in the extent of back-

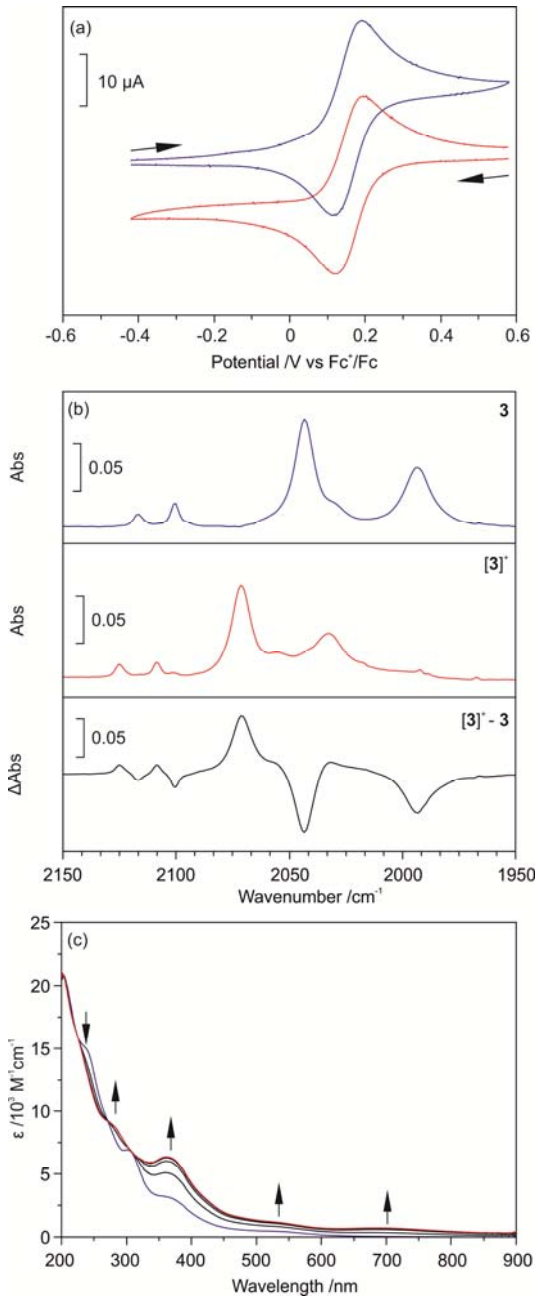

Figure 4: (a) Cyclic voltammograms of **3** (1 mM) at 253 K before (blue line) and after electrochemical oxidation (red line); (b) absorbance IR spectra of **3** (top) and electrochemically generated $[\mathbf{3}]^+$ (middle), and the difference IR spectrum of $[\mathbf{3}]^+$ and **3** (bottom); (c) electronic spectra for the one electron oxidation of a solution of **3** (2 mM) at 253 K. All experiments were carried out as MeCN solutions with 0.2 M $[N^nBu_4][BF_4]$ as supporting electrolyte.

donation to the π* anti-bonding combinations of the CO and CN^- ligands. The average shift of $\Delta\nu_{CN}$ [~ 9 cm^{-1}] is smaller than that of $\Delta\nu_{CO}$ [~ 35 cm^{-1}], which reflects the higher sensitivity of the CO ligands to electronic changes about the metal center as compared to the CN^- ligands.[42] The relative shifts of ν_{CO} and ν_{CN} are consistent with those observed between the Ni^{II}-SIa (formally Ni^{II}) and Ni^{III}-C (formally Ni^{III}) states of the [NiFe] hydrogenase from *D. vulgaris* Miyazaki F ($\Delta\nu_{CN}$ *ca.* 1 cm^{-1} and $\Delta\nu_{CO}$ *ca.* 18 cm^{-1}).[43]

The one-electron oxidation of **3** was also monitored by UV/vis spectroelectrochemistry in MeCN solution containing 0.2 M $[N^nBu_4][BF_4]$ as supporting electrolyte at 253 K in an optically transparent electrode OTE cell [Figure 4(c)]. The oxidation of **3** at 0.5 V *vs* Fc^+/Fc is associated with a decrease in the intensity of the absorbance of the bands assigned to **3** and the development of new absorption features attributed to $[\mathbf{3}]^+$. The presence of isosbestic points [Figure 4(c) and Table S1] indicates that the electrochemical oxidation of **3** occurs with no long-lived intermediates. The electrochemical reduction of $[\mathbf{3}]^+$ led to the quantitative regeneration of the UV/vis spectrum of **3**, confirming the chemical reversibility of the oxidation process over the timescale of the UV/vis spectroelectrochemical experiment. The X-band EPR spectrum of electrochemically generated $[Ni(L^3)]^+$ was recorded at 77 K in MeCN solution with 0.2 M $[N^nBu_4][BF_4]$ as supporting electrolyte and may be simulated as a doublet (S = ½) species with spin Hamiltonian parameters g_{33} = 2.238, g_{22} = 2.112 g_{11} = 2.037 (Figure 5, Table 4). The relatively high g-anisotropy with $g_{av} \neq g_e$ is consistent with an unpaired electron that is localized principally on a transition metal, *i.e.*, $[Ni(L^3)]^+$ may be formulated as a formal Ni^{III} center.[44] A $3d^7$ S = ½ center in a regular square-based pyramidal environment possesses an axial EPR spectrum with $g_\perp > g_\parallel$.[45] Thus, the rhombic X-band frozen solution EPR spectrum of $[Ni(L^3)]^+$ is most likely associated with the distortion of the ligand sphere within the equatorial plane away from the essentially square pyramidal geometry of $[Ni(L^3)]$, as revealed by DFT calculations on $[Ni(L^3)]^+$ (see Supplementary Information).

The electrochemical oxidation of **3** to [**3**]$^+$ in MeCN solution containing 0.2 M [N^nBu_4][BF_4] as supporting electrolyte results in a frozen solution X-band EPR spectrum that may be simulated as an S = ½ center with spin Hamiltonian parameters g_{33} = 2.163, g_{22} = 2.129 and g_{11} = 2.014 (Figure 5, Table 4). The magnitude of the smallest *g* value ($g_{33} \approx g_e$) suggests that [**3**]$^+$ contains a formal Ni^{III} center in which one unpaired electron resides primarily in a $3d_{z^2}$ orbital.[1c,46] The frozen solution EPR spectrum of [**3**]$^+$ possesses less anisotropy than that of [Ni(L^3)]$^+$, which is most likely due to the {$Fe(CO)_2(CN)_2$} fragment bound through thiolate S donors to the {NiN_2S_3} unit. This co-ordination may limit distortion about the {NiN_2S_3} fragment and support a more ideal square-base pyramidal geometry about the Ni center following the oxidation of **3**. The rhombic spin Hamiltonian parameters of [**3**]$^+$ are similar to those of the paramagnetic $Ni^{III}Fe^{II}$ (Ni-C) state of the [NiFe] hydrogenase from *D. gigas* (Table 4) that have been assigned to a $(3d_{z^2})^1$ ground state.[46-47]

Preliminary studies suggest that **3** and electrochemically prepared [**3**]$^+$ show no activity with respect to H_2 evolution or H_2 consumption following treatment with CF_3COOH and H_2, respectively. We ascribe this to the saturated co-ordination sphere about the Fe center in **3** and [**3**]$^+$.

Table 4: Experimental and calculated principal components of the *g*-tensor for [Ni(L^3)]$^+$ and [**3**]$^+$, and the experimental *g*-values of the Ni-A, Ni-B and Ni-C states of [NiFe] hydrogenase from *D. gigas*.[6g]

	g_{33}	g_{22}	g_{11}	g_{33}-g_{11}
[Ni(L^3)]$^+$ Experimental	2.238	2.112	2.037	0.201
[Ni(L^3)]$^+$ Calculated B3LYP $<S^2>$ = 0.846	2.288	2.211	2.095	0.193
[Ni(L^3)]$^+$ Calculated PBE0 $<S^2>$ = 0.951	2.280	2.252	2.010	0.270
[Ni(L^3)]$^+$ Calculated BP86 $<S^2>$ = 0.769	2.175	2.132	2.032	0.143
[**3**]$^+$ Experimental	2.165	2.128	2.014	0.151
[**3**]$^+$ Calculated B3LYP $<S^2>$ = 0.795	2.231	2.206	2.062	0.169
[**3**]$^+$ Calculated PBE0 $<S^2>$ = 0.851	2.339	2.255	2.137	0.202
[**3**]$^+$ Calculated BP86 $<S^2>$ = 0.760	2.143	2.117	2.028	0.115
Ni-A	2.31	2.23	2.01	
Ni-B	2.33	2.16	2.01	
Ni-C	2.19	2.16	2.01	

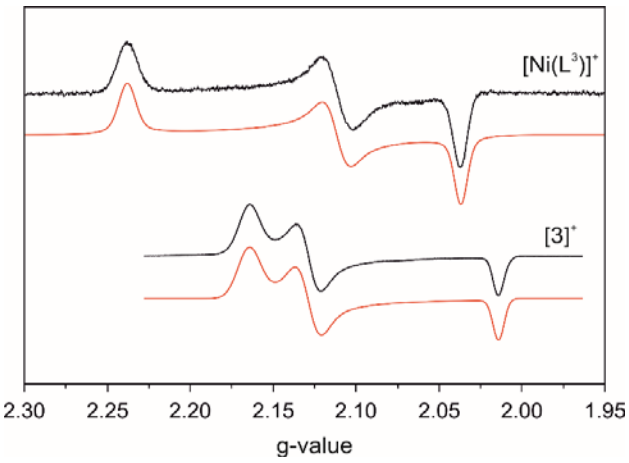

Figure 5: Frozen solution X-band EPR spectrum of $[\mathbf{3}]^{+}$ and $[Ni(L^3)]^{+}$ and in MeCN solution with 0.2 M $[N^nBu_4][BF_4]$ as supporting electrolyte. Experimental (black) and simulated (red) spectra using parameters $g_{33} = 2.163$, $g_{22} = 2.129$ and $g_{11} = 2.014$ for $[\mathbf{3}]^{+}$, and $g_{33} = 2.238$, $g_{22} = 2.112$ and $g_{11} = 2.037$ for $[Ni(L^3)]^{+}$.

DFT calculations

We undertook DFT calculations models of $[\mathbf{3}]^{+/0}$ and $[Ni(L^3)]^{+/0}$ to gain insight into the electronic structures of these centers and to provide a framework within which to interpret the X-ray crystallographic and spectroscopic results. A comparison on the metrical parameters of $[Ni(L^3)]$ derived from X-ray crystallography[34c] and from DFT calculations is consistent with the assignment of a singlet (S = 0) configuration in the solid state structure of $[Ni(L^3)]$ (see Supplementary Information).

Selected metrical parameters for gas-phase, geometry optimized models of **3** in the S = 0 and S = 1 states are shown in Table 1 and the calculated structures are shown in Figure S7. **3** (S = 1) features a Ni center in an approximate square pyramidal environment with the thioether S donor located at the apical position at a distance [Ni(1)-S(3) = 2.350 Å] that is within *ca.* 0.02 Å of the corresponding distances in **3**A and **3**B. The DFT optimized structure of **3** (S = 1) underestimates the Ni(1)-S(3) distance in **3**C [Ni(1)-S(3) = 2.6856(19) Å] by *ca.* 0.34 Å. In contrast gas-phase geometry optimizations

of **3** (S = 0) reproduce the Ni(1)-S(3) distance in **3**C to within *ca.* 0.08 Å. DFT calculations for **3** (S = 0) and **3** (S = 1) overestimate the Ni(1)-S(1)/S(2) and Ni(1)-N(3)/N(4) distances in **3**A and **3**B (S = 1) and **3**C (S = 0) by *ca.* 0.04 - 0.07 Å. However, the calculations suggest that the shortening of the Ni(1)-S(3) distance in **3** (S = 1) is accompanied by a simultaneous relaxation of the average Ni(1)-S(1)/S(2) and Ni(1)-N(3)/N(4) distances [2.323 Å and 2.160 Å, respectively]. The average Ni(1)-S(1)/S(2) and Ni(1)-N(3)/N(4) distances [2.213 Å and 2.007 Å, respectively] appear to shorten as the Ni(1)-S(3) distance lengthens in **3** (S = 0). Based on these observations, the model **3** (S = 1) shows a correspondence with the structures **3**A and **3**B, which consequently are assigned to the triplet (S = 1) state. In contrast, **3**C approaches the calculated structure of **3** (S = 0). It should be noted, however, that the model of **3** (S = 0) overestimates the Ni(1)-S(3) distance as determined by X-ray crystallography by *ca*. 0.08 Å. This represents a greater difference in the Ni(1)-S(3) distance for the calculated geometry of **3** (S = 1) as compared to the experimental Ni(1)-S(3) distances in **3**A and **3**B (Table 1). This may suggest that **3**C represents an intermediate between the S = 1 and 0 spin states that approaches the S = 0 limit. There is no significant trigonal distortion for the $\{NiN_2S_3\}$ unit in the experimental **3**A, **3**B, **3**C and calculated **3** (S = 0) and **3** (S = 1) structures; each may be described as possessing a similar distorted square-pyramidal geometry ($\tau = 0.14 – 0.18$). **3** (S = 1) is 4.57 kcal mol^{-1} lower in energy than **3** (S = 0) and the geometry of the $\{Fe(CO)_2(CN)_2\}$ unit remains essentially invariant between the **3** (S = 0) and **3** (S = 1) structures.

The gas-phase geometry optimized structure of $[\mathbf{3}]^+$ broadly retains the geometrical features calculated for **3** (S = 1) (Table 1, Figure S7). The Ni center adopts a distorted square-pyramidal geometry with Ni(1)-S(3) = 2.395 Å and $\tau = 0.16$. The Fe center maintains a distorted octahedral geometry with only a small variation (*ca.* 2º) in the C(1)-Fe(1)-C(4) and C(2)-Fe(1)-C(3) angles in **3** and $[\mathbf{3}]^+$. The absence of significant structural differences for **3** and $[\mathbf{3}]^+$ is consistent with the

electrochemical reversibility observed experimentally for the $[\mathbf{3}]^{+/0}$ redox process. The calculated IR ν_{CN} and ν_{CO} frequencies for **3** (S = 0), **3** (S = 1) and $[\mathbf{3}]^+$ and the experimental data for **3** and $[\mathbf{3}]^+$ are shown in Table 5. The asymmetric ν_{CO} frequency is well reproduced for **3** (S = 0) (1991 cm^{-1} calculated *vs.*1993 cm^{-1} experimental) while for **3** (S = 1) there is a greater difference (*ca*. 5 cm^{-1}) between the calculated and experimental frequencies. However, the difference between the calculated ν_{CN} and the calculated symmetric ν_{CO} frequencies of **3** (S = 1) and **3** (S = 0) is small. For **3** (S = 1) and **3** (S = 0) the symmetric ν_{CO} frequency is underestimated by *ca*. 10 cm^{-1} and the separation between the two CN bands is overestimated ($\Delta\nu_{CN}$ 45 cm^{-1} *vs.*17 cm^{-1} from the experimental data). Thus, a comparison of the calculated and experimental ν_{CN} and ν_{CO} frequencies alone cannot unambiguously confirm the spin state of **3** in solution, however we note that the ^{1}H NMR spectra of **3** and [Ni(L^3)] are broad suggesting that **3** and [Ni(L^3)] are in triplet (S = 1) states as CD_3CN solutions. The ν_{CN} and ν_{CO} frequencies calculated for $[\mathbf{3}]^+$ show an overall shift of *ca.* 22 cm^{-1} relative to those calculated for **3** (S = 1) and *ca.* 24 cm^{-1} relative to those calculated for **3** (S = 0). These shifts compare well to those observed experimentally (*ca.* is 21 cm^{-1}) between **3** and $[\mathbf{3}]^+$ [Figure 4(b) and Table 5].

Table 5: Gas-phase calculated and experimental IR ν_{CN} and ν_{CO} frequencies for **3** and $[\mathbf{3}]^+$in MeCN solution with 0.2 M $[N^nBu_4][BF_4]$ as supporting electrolyte.

	3 (S = 0) Calc.	**3** (S = 1) Calc.	**3** Exp.	$[\mathbf{3}]^+$ Calc.	$[\mathbf{3}]^+$ Exp.
ν_{CN} /cm^{-1}	2132	2135	2117	2141	2125
	2088	2087	2100	2096	2108
ν_{CO} /cm^{-1}	2031	2033	2043	2064	2071
	1991	1998	1993	2037	2033

DFT calculations employing the B3LYP and PBE0 functionals generally overestimate the principal values of the *g*-tensor for $[Ni(L^3)]^+$ where the levels of spin contamination, as revealed by $\langle S^2 \rangle$, make these estimates unreliable (Table 4). Similar levels of spin contamination have been reported previously in calculations on the Ni-L state of the [NiFe] hydrogenases employing the B3LYP

functional.[48] Consequently we chose to calculate spin Hamiltonian parameters using the BP86 functional where spin contamination is negligible. In these calculations g_{33} is underestimated (Table 4) and similar underestimations (by up to 30%) have been observed previously with this functional and have been attributed partly to overestimations in spin delocalization into ligand-based orbitals.[48-49] Nevertheless, the calculations reproduce the lower anisotropy associated with the *g*-tensor of [**3**]$^+$, as measured by g_{33}-g_{11}, relative to that of [Ni(L^3)]$^+$ (Experimental g_{33}-g_{11} = 0.201 and 0.151 for [**3**]$^+$ and [Ni(L^3)]$^+$, respectively, Table 4). This difference in anisotropy mirrors the smaller trigonal distortion of the {NiN_2S_3} unit in [**3**]$^+$ (τ = 0.16) relative to that in [Ni(L^3)]$^+$ (τ = 0.41, Tables 1 and S2).

The β-spin LUMO (141β) of [**3**]$^+$ corresponds to the formally singly occupied molecular orbital (SOMO) with its α-spin counterpart (133α) occupied. Natural population analysis[50] reveals that the β-spin LUMO possesses Ni [55.8% total with Ni $3d_{z^2}$ (45.6%) and $3d_{xz}$ (8.3%)], S [6.1% total S(1), 6.5% total S(2) and 21.2% total S(3)] and Fe [1.2% total with Fe $3d_{xz}$ (0.2%) and $3d_{x^2-y^2}$ (1.0%)] character. This composition is consistent with the calculated spin density for [**3**]$^+$ (Figure 6) that lies principally across the Ni and S(3) centers. Thus, the calculations suggest that the co-ordination of an {$Fe(CO)_2(CN)_2$} fragment to the {NiN_2S_3} unit substantially decreases the equatorial thiolate S character in the SOMO from 22.5% in [Ni(L^3)]$^+$ (see Supplementary Information) to 12.6% in [**3**]$^+$.

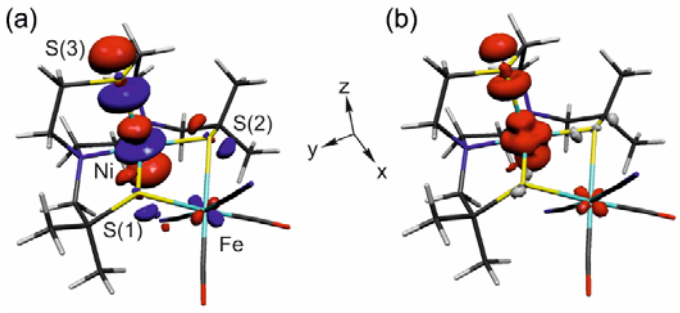

Figure 6: (a) The calculated β-spin LUMO for [**3**]$^+$ with an isosurface value of 0.05 e Å^{-3} and (b) the spin density distribution for [**3**]$^+$ with an isosurface value of 0.005 e Å^{-3}.

The geometry of the Ni site in Ni-C may be described as approximately square-based pyramidal in which the base plane is formed from three CysS donors and the bridging hydride, and the apical position is occupied by the remaining CysS donor.[46] An analysis of the *g*-tensor for the Ni-C state of the [NiFe] hydrogenase from *D. vulgaris* Miyazaki F, supported by DFT calculations, reveals a formal Ni^{III} $3d_{z^2}$ ground state in which there is significant delocalization of spin into the 3*p* orbital of the apical Cys549 S-donor together with some delocalization onto the equatorial Cys546 S-donor.[47] In these respects the electronic structure of $[\mathbf{3}]^+$ shows a close correspondence to that proposed for the Ni-C state of the [NiFe] hydrogenases *i.e.* an essentially Ni^{III} $3d_{z^2}$ ground state with significant delocalization of spin onto the apical S-donor, which is derived from the thioether group in $[\mathbf{3}]^+$.

Conclusions

We have synthesized and characterized the binuclear [NiFe] complexes **1** – **3** as analogs of the active sites of the [NiFe] hydrogenases and extended the range of [NiFe] complexes incorporating an Fe center with a mixed CO and CN^- ligand set. The X-ray crystallographic structures of **1** – **3** sample two of the four possible isomers, namely *trans*-CN and *cis*-CN_{endo}, that result from the butterfly shape of the $\{NiFe_2\}$ core and the arrangement of two CO and two CN^- ligands about the Fe center (Scheme 3). The co-ordination of two CO ligands in the metal cluster of **1** – **3** makes the formulation of these centers similar to that proposed for the CO-inhibited Ni-SCO state of the [NiFe] hydrogenase from *D. vulgaris* Miyazaki F.[51] However, in Ni-SCO the second CO ligand co-ordinates to the Ni center rather than the Fe center as found for **1** – **3**. Moreover, the two CO ligands in **1** – **3** occupy positions away from the Ni-center with only the CN^- defined by C(1) (Figure 2) directed towards the Ni(1) atom. The Ni(1)-C(1) distances in **1** – **3** [2.923(5) to 3.140(7) Å, Table 1] suggest that this CN^- is not bound to the Ni(1) center and co-ordinates to the Fe(1) center only. While $(CO)_3Fe(\mu\text{-}S^tBu)_3Ni\{SC_6H_3\text{-}2,6\text{-}(mesityl)_2\}$ shows CO

binding at the Ni center,[52] the majority of analogs of the Ni-SCO form of the [NiFe] hydrogenases contain CO bound to M in heterodinuclear [$Ni^{II}M$] (M = Fe^{II}, Ru^{II} or Ir^{III}) complexes.[6n,53] These observations suggest an alternative mechanism for the inhibition of H_2 oxidation activity in [NiFe] hydrogenases through co-ordination of a second CO ligand to the Fe^{II} center at the active site.[53a] Our results appear to support this mechanism in which two CO and two CN^- ligands co-ordinate the Fe(1) center in **1** – **3**, with no interactions of these ligands with the adjacent Ni(1) atom being observed.

1 - **3** exhibit irreversible reduction processes in the range of −1.67 to −1.45 V *vs* Fc^+/Fc that are associated with the generation of unstable species. These were not investigated further. The reversible oxidation of **3** is localized about the Ni center and involves a redox active orbital that is essentially Ni $3d_{z^2}$ and S(3)-based showing a close correspondence with the SOMO calculated for the Ni-C state of the [NiFe] hydrogenase from *D. vulgaris* Miyazaki F.[47] The DFT calculations and the EPR spectroscopic signature of [**3**]$^+$ are consistent with an assignment of [**3**]$^+$ to a formal $Ni^{III}Fe^{II}$ center that mirrors that of the Ni-C state.[46-47]

The SOMO of [Ni(L^3)]$^+$ possesses significantly more equatorial S-character than that in [**3**]$^+$ (22.5% *vs.* 12.6%, respectively). Thus, the co-ordination of an {$Fe(CO)_2(CN)_2$} fragment to [Ni(L^3)]$^+$ in [**3**]$^+$ appears to limit thiyl radical contributions derived from the equatorial S donors in the SOMO. This suggests that the co-ordination of the {$Fe(CO)(CN)_2$} unit to the $Ni(CysS)_4$ center in the Ni-C state of the [NiFe] hydrogenases may also play a similar role to ensure that the spin density is localized across the Ni and apical CysS centers. This would represent an alternative strategy for controlling the electronic structures of Ni centers bound by CysS ligands in biology. Thus, it has been proposed that the unusual square planar N_2S_2 co-ordination sphere at the active sites of the Ni-containing superoxide dismutases (NiSODs),[54] together with the co-ordination of a N donor derived from His1 at the axial position in the oxidized form, promotes a Ni^{III} center with a formal $3d_{z^2}$ ground state.[55] This has the effect of

suppressing thiolate-based oxidative chemistry that could result in the formation of sulfonate groups which may inactivate the enzyme. In addition, the co-ordination of the $\{Fe(CO)_2(CN)_2\}$ fragment to $[Ni(L^3)]$ in **3** may suppress significant changes in the geometry of the $[Ni(L^3)]$ unit on oxidation as well as modulating the redox potential of the $[\mathbf{3}]^{+/0}$ couple. The $\{Fe(CO)(CN)_2\}$ center may play similar roles at the active site of the [NiFe] hydrogenases in addition to supporting a bridging hydride species between the Ni and Fe centers in the Ni-C state.[1c,56]

Associated content

The Supporting Information contains Figures S1 – S8 and Tables S1 – S18. CCDC 1584099-1584102 contain the supplementary crystallographic data for this paper. These data can be obtained free of charge via www.ccdc.cam.ac.uk/data_request/cif, or by emailing data_request@ccdc.cam.ac.uk, or by contacting The Cambridge Crystallographic Data Centre, 12 Union Road, Cambridge CB2 1EZ, UK; fax: +44 1223 336033.

Author Information

Corresponding Author

*E-mail: j.mcmaster@nottingham.ac.uk

*E-mail: m.schroder@manchester.ac.uk

Acknowledgements

We thank Dr J. Jiang for discussions relating to the synthesis of *fac*-K[$Fe(CN)_2(CO)_3I$].[9a] We thank EPSRC and the University of Nottingham for support. We are grateful for access to the University of Nottingham High Performance Computing Facility. MS gratefully acknowledges receipt of an ERC Advanced Grant (AdG 226593).

References

1. (a) Fontecilla-Camps, J. C.; Volbeda, A.; Cavazza, C.; Nicolet, Y. Structure/Function Relationships of [NiFe]- and [FeFe]-Hydrogenases. *Chem. Rev.* **2007,** *107*, 4273-4303; (b) Fontecilla-Camps, J. C.; Volbeda, A.; Frey, M. Hydrogen Biocatalysis: A Tale of Two Metals. *Trends Biotechnol.* **1996,** *14*, 417-420; (c) Lubitz, W.; Ogata, H.; Rüdiger, O.; Reijerse, E. Hydrogenases. *Chem. Rev.* **2014,** *114*, 4081-4148; (d) Ogata, H.; Lubitz, W.; Higuchi, Y. Structure and Function of NiFe Hydrogenases. *J. Biochem.* **2016,** *160*, 251-258.
2. Ogata, H.; Lubitz, W.; Higuchi, Y. [NiFe] Hydrogenases: Structural and Spectroscopic Studies of the Reaction Mechanism. *Dalton Trans.* **2009,** *9226*, 7577-87.
3. Canaguier, S.; Artero, V.; Fontecave, M. Modelling NiFe Hydrogenases: Nickel-Based Electrocatalysts for Hydrogen Production. *Dalton Trans.* **2008,** *25*, 315-325.
4. Siegbahn, P. E. M.; Blomberg, M. R. A.; Wirstam née Pavlov, M.; Crabtree, R. H. The Mechanism of the Ni-Fe Hydrogenases: A Quantum Chemical Perspective. *J. Biol. Inorg. Chem.* **2001,** *6*, 460-466.
5. Hidalgo, R.; Ash, P. A.; Healy, A. J.; Vincent, K. A. Infrared Spectroscopy During Electrocatalytic Turnover Reveals the Ni-L Active Site State During H_2 Oxidation by a NiFe Hydrogenase. *Angew. Chem. Int. Ed.* **2015,** *54*, 7110-7113.
6. (a) Dawson, J.; Ghiotto, F.; McMaster, J.; Schroder, M., Metal Complex of Hydrogenase Active Sites. In *Molecular Solar Fuels*, Wydrzynski, T. J.; Hillier, W., Eds. 2011; pp 326-386; (b) Dawson, J.; Perotto, C.; McMaster, J.; Schröder, M., [NiFe] Hydrogenases. In *Bioinspired Catalysis*, Wiley-VCH Verlag GmbH & Co. KGaA: Weinheim, Germany, 2014; pp 49-78; (c) Helm, M. L.; Stewart, M. P.; Bullock, R. M.; DuBois, M. R.; DuBois, D. L. A Synthetic Nickel Electrocatalyst with a Turnover Frequency Above 100,000 s^{-1} for H_2 Production. *Science* **2011,** *333*, 863-866; (d) Lai, C.

H.; Reibenspies, J. H.; Darensbourg, M. Y. Thiolate Bridged Nickel-iron Complexes Containing Both Iron(0) and Iron(II) Carbonyls. *Angew. Chem. Int. Ed.* **1996,** *35*, 2390-2393; (e) Ogo, S.; Ichikawa, K.; Kishima, T.; Matsumoto, T.; Nakai, H.; Kusaka, K.; Ohhara, T. A Functional [NiFe]Hydrogenase Mimic That Catalyzes Electron and Hydride Transfer from H_2. *Science* **2013,** *339*, 682-684; (f) Summers, P. A.; Dawson, J.; Ghiotto, F.; Hanson-Heine, M. W. D.; Vuong, K. Q.; Davies, E. S.; Sun, X.-Z.; Besley, N. A.; McMaster, J.; George, M. W.; Schröder, M. Photochemical Dihydrogen Production Using an Analogue of the Active Site of [NiFe] Hydrogenase. *Inorg. Chem.* **2014,** *53*, 4430-4439; (g) Tard, C.; Pickett, C. J. Structural and Functional Analogues of the Active Sites of the Fe -, NiFe -, and FeFe -Hydrogenases. *Chem. Rev.* **2009,** *109*, 2245-2274; (h) Weber, K.; Kraemer, T.; Shafaat, H. S.; Weyhermueller, T.; Bill, E.; van Gastel, M.; Neese, F.; Lubitz, W. A Functional NiFe -Hydrogenase Model Compound That Undergoes Biologically Relevant Reversible Thiolate Protonation. *J. Am. Chem. Soc.* **2012,** *134*, 20745-20755; (i) Nguyen, N. T.; Mori, Y.; Matsumoto, T.; Yatabe, T.; Kabe, R.; Nakai, H.; Yoon, K.-S.; Ogo, S. A NiFe Hydrogenase Model that Catalyses the Release of Hydrogen from Formic Acid. *Chem. Commun.* **2014,** *50*, 13385-13387; (j) Wombwell, C.; Reisner, E. Synthetic Active Site Model of the NiFeSe Hydrogenase. *Chem. Eur. J.* **2015,** *21*, 8096-8104; (k) Artero, V.; Berggren, G.; Atta, M.; Caserta, G.; Roy, S.; Pecqueur, L.; Fontecave, M. From Enzyme Maturation to Synthetic Chemistry: The Case of Hydrogenases. *Acc. Chem. Res.* **2015,** *48*, 2380-2387; (l) Brazzolotto, D.; Gennari, M.; Queyriaux, N.; Simmons, T. R.; Pecaut, J.; Demeshko, S.; Meyer, F.; Orio, M.; Artero, V.; Duboc, C. Nickel-Centred Proton Reduction Catalysis in a Model of NiFe Hydrogenase. *Nat. Chem.* **2016,** *8*, 1054-1060; (m) Eberhardt, N. A.; Guan, H. Nickel Hydride Complexes. *Chem. Rev.* **2016,** *116*, 8373-8426; (n) Ogo, S.; Mori, Y.; Ando, T.; Matsumoto, T.; Yatabe, T.; Yoon, K.-S.; Hayashi, H.; Asano, M. One Model, Two Enzymes: Activation of Hydrogen and Carbon Monoxide. *Angew.*

Chem. Int. Ed. **2017,** *56*, 9723-9726; (o) Schilter, D.; Camara, J. M.; Huynh, M. T.; Hammes-Schiffer, S.; Rauchfuss, T. B. Hydrogenase Enzymes and Their Synthetic Models: The Role of Metal Hydrides. *Chem. Rev.* **2016,** *116*, 8693-8749; (p) Xu, T.; Chen, D.; Hu, X. Hydrogen-activating Models of Hydrogenases. *Coord. Chem. Rev.* **2015,** *303*, 32-41.

7. Jiang, J. F.; Koch, S. A. *fac*-$[Fe^{II}(CN)_3(CO)_3]^-$ and *cis*-$[Fe^{II}(CN)_4(CO)_2]^{2-}$: New Members of the Class of $[Fe^{II}(CN)_x(CO)_y]$ Compounds. *Inorg. Chem.* **2002,** *41*, 158-160.
8. Kruger, H. J.; Peng, G.; Holm, R. H. Low-potential Nickel(III,II) Complexes: New Systems Based on Tetradentate Amidate-thiolate Ligands and the Influence of Ligand Structure on Potentials in Relation to the Nickel Site in [NiFe]-Hydrogenases. *Inorg. Chem.* **1991,** *30*, 734-742.
9. (a) Jiang, J.; Maruani, M.; Solaimanzadeh, J.; Lo, W.; Koch, S. A.; Millar, M. Synthesis and Structure of Analogues for the NiFe Site in Hydrogenase Enzymes. *Inorg. Chem.* **2009,** *48*, 6359-6361; (b) Li, Z.; Ohki, Y.; Tatsumi, K. Dithiolato-bridged Dinuclear Iron-Nickel Complexes $[Fe(CO)_2(CN)_2(\mu\text{-}SCH_2CH_2CH_2S)Ni(S_2CNR_2)]$- Modeling the Active Site of [NiFe] Hydrogenase. *J. Am. Chem. Soc.* **2005,** *127*, 8950-8951; (c) Manor, B. C.; Rauchfuss, T. B. Hydrogen Activation by Biomimetic [NiFe]-Hydrogenase Model Containing Protected Cyanide Cofactors. *J. Am. Chem. Soc.* **2013,** *135*, 11895-11900; (d) Tanino, S.; Li, Z.; Ohki, Y.; Tatsumi, K. A Dithiolate-bridged $(CN)_2(CO)$Fe-Ni Complex Reproducing the IR Bands of [NiFe] Hydrogenase. *Inorg. Chem.* **2009,** *48*, 2358-2360.
10. (a) Barton, B. E.; Whaley, C. M.; Rauchfuss, T. B.; Gray, D. L. Nickel-Iron Dithiolato Hydrides Relevant to the [NiFe]-Hydrogenase Active Site. *J. Am. Chem. Soc.* **2009,** *131*, 6942-6943; (b) Zhu, W.; Marr, A. C.; Wang, Q.; Neese, F.; Spencer, D. J. E.; Blake, A. J.; Cooke, P. A.; Wilson, C.; Schröder, M. Modulation of the Electronic Structure and the Ni-Fe Distance in Heterobimetallic

Models for the Active Site in [NiFe] Hydrogenase. *Proc. Nat. Acad. Sci. U.S.A.* **2005,** *102*, 18280-18285.

11. (a) Chambers, G. M.; Huynh, M. T.; Li, Y. L.; Hammes-Schiffer, S.; Rauchfuss, T. B.; Reijerse, E.; Lubitz, W. Models of the Ni-L and Ni-Sl_a States of the NiFe -Hydrogenase Active Site. *Inorg. Chem.* **2016,** *55*, 419-431; (b) Perotto, C. U.; Marshall, G.; Jones, G. J.; Stephen Davies, E.; Lewis, W.; McMaster, J.; Schröder, M. A Ni(I)Fe(II) Analogue of the Ni-L State of the Active Site of the [NiFe] Hydrogenases. *Chem. Commun.* **2015,** *51*, 16988-91.
12. Chambers, G. M.; Mitra, J.; Rauchfuss, T. B.; Stein, M. Ni^{I}/Ru^{II} Model for the Ni–L State of the [NiFe]Hydrogenases: Synthesis, Spectroscopy, and Reactivity. *Inorg. Chem.* **2014,** *53*, 4243-4249.
13. SADABS. Bruker AXS Inc., Madison, Wisconsin, USA, 2001.
14. CrysAlis PRO, Agilent Technologies, Yarnton, England 2010.
15. Sheldrick, G. M. A Short History of SHELX. *Acta Crystallogr., Sect. A* **2008,** *64*, 112-122.
16. Bourhis, L. J.; Dolomanov, O. V.; Gildea, R. J.; Howard, J. A. K.; Puschmann, H. The Anatomy of a Comprehensive Constrained, Restrained Refinement Program for the Modern Computing Environment – Olex2 Dissected. *Acta. Crystallogr., Sec. A* **2015,** *A71*, 59-75.
17. Sheldrick, G. M. Crystal Structure Refinement with SHELXL. *Acta Crystallogr., Sect. C* **2015,** *C71*, 3-8.
18. Spek, A. L. Structure Validation in Chemical Crystallography. *Acta Crystallogr., Sect. D* **2009,** *65*, 148-155.
19. Frisch, M. J.; Trucks, G. W.; Schlegel, H. B.; Scuseria, G. E.; Robb, M. A.; Cheeseman, J. R.; Montgomery, J., J. A.;; Vreven, T.; Kudin, K. N.; Burant, J. C.; Millam, J. M.; Iyengar, S. S.; Tomasi, J.; Barone, V.; Mennucci, B.; Cossi, M.; Scalmani, G.; Rega, N.; Petersson, G. A.; Nakatsuji, H.; Hada, M.; Ehara, M.; Toyota, K.; Fukuda, R.; Hasegawa, J.; Ishida, M.; Nakajima,

T.; Honda, Y.; Kitao, O.; Nakai, H.; Klene, M.; Li, X.; Knox, J. E.; Hratchian, H. P.; Cross, J. B.; Bakken, V.; Adamo, C.; Jaramillo, J.; Gomperts, R.; Stratmann, R. E.; Yazyev, O.; Austin, A. J.; Cammi, R.; Pomelli, C.; Ochterski, J. W.; Ayala, P. Y.; Morokuma, K.; Voth, G. A.; Salvador, P.; Dannenberg, J. J.; Zakrzewski, V. G.; Dapprich, S.; Daniels, A. D.; Strain, M. C.; Farkas, O.; Malick, D. K.; Rabuck, A. D.; Raghavachari, K.; Foresman, J. B.; Ortiz, J. V.; Cui, Q.; Baboul, A. G.; Clifford, S.; Cioslowski, J.; Stefanov, B. B.; Liu, G.; Liashenko, A.; Piskorz, P.; Komaromi, I.; Martin, R. L.; Fox, D. J.; Keith, T.; Al-Laham, M. A.; Peng, C. Y.; Nanayakkara, A.; Challacombe, M.; Gill, P. M. W.; Johnson, B.; Chen, W.; Wong, M. W.; Gonzalez, C.; Pople, J. A., Gaussian 03, Revision D.01. Gaussian, Inc., Wallingford CT, 2004.

20. (a) Becke, A. D. Density-Functional Exchange-Energy Approximation with Correct Asymptotic Behavior. *Phys. Rev. A,* **1988,** *38*, 3098–3100; (b) Perdew, J. Density-functional Approximation for the Correlation Energy of the Inhomogeneous Electron Gas. *Phys. Rev. B* **1986,** *33*, 8822-8824.
21. Becke, A. D. Density-Functional Thermochemistry. III. The Role of Exact Exchange. *J. Chem. Phys.* **1993,** *98*, 5648–5652.
22. Lee, C.; Yang, W.; Parr, R., G. Development of the Colle-Salvetti Correlation-energy Formula into a Functional of the Electron Density. *Phys. Rev. B.* **1988,** *37*, 785–789.
23. Pardo, A.; De Lacey, A. L.; Fernández, V. M.; Fan, H.-J.; Fan, Y.; Hall, M. B. Density Functional Study of the Catalytic Cycle of Nickel-iron [NiFe] Hydrogenases and the Involvement of High-spin Nickel(II). *J. Biol. Inorg. Chem.* **2006,** *11*, 286-306.
24. Hay, P. J.; Wadt, W. R. *Ab Initio* Effective Core Potentials for Molecular Calculations. Potentials for K to Au Including the Outermost Core Orbitals. *J. Chem. Phys.* **1985,** *82*, 299-310.
25. Couty, M.; Hall, M. B. Basis Sets for Transition Metals: Optimized Outer *p* Functions. *J. Comput. Chem.* **1996,** *17*, 1359-1370.

26. Ehlers, A. W.; Biihme, M.; Dapprich, S.; Gobbi, A.; Hijllwarth, A.; Jonas, V.; Kiihler, K. F.; Stegmann, R.; A., V.; Frenking, G. A Set of f-Polarization Functions for Pseudo-potential Basis Sets of the Transition Metals Sc-Cu, Y-Ag and La-Au. *Chem. Phys. Lett.* **1993,** *208*, 111-114.
27. Check, C. E.; Faust, T. O.; Bailey, J. M.; Wright, B. J.; Gilbert, T. M.; Sunderlin, L. S. Addition of Polarization and Diffuse Functions to the LANL2DZ Basis Set for P-Block Elements. *J. Phys. Chem. A* **2001,** *105*, 8111-8116.
28. Grev, R. S.; Schaefer III, H. F. 6-311G is Not of Valence Triple-zeta Quality. *J. Chem. Phys.* **1989,** *91*, 7305-7306.
29. (a) Bauschlicher, C. W.; Langhoff, S. R.; Partridge, H.; Barnes, L. A. Theoretical Studies of the First- and Second-row Transition-metal Methyls and their Positive Ions. *J. Chem. Phys.* **1989,** *91*, 2399-2411; (b) Krishnan, R.; Binkley, J. S.; Seeger, R.; Pople, J. A. Self-consistent Molecular Orbital Methods. XX. A Basis Set for Correlated Wave Functions. *J. Chem. Phys.* **1980,** *72*, 650-654; (c) McLean, A. D.; Chandler, G. S. Contracted Gaussian Basis Sets for Molecular Calculations. I. Second Row Atoms, Z=11–18. *J. Chem. Phys.* **1980,** *72*, 5639-5648.
30. Barone, V., Structure, Magnetic Properties and Reactivities of Open-Shell Species from Density Functional and Self-Consistent Hybrid Methods. In *Recent Advances in Density Functional Methods, Part I*, Chong, D. P., Ed. World Scientific Publ. Co.: Singapore, 1996.
31. Portmann, S.; Lüthi, H. P. MOLEKEL: An Interactive Molecular Graphics Tool. *Chimia (Aarau)* **2000,** *6*, 766–770.
32. Lu, T.; Chen, F. Multiwfn: a Multifunctional Wavefunction Analyzer. *J. Comp. Chem.* **2012,** *33*, 580-592.
33. Glendening, E. D.; Reed, A. E.; Carpenter, J. E.; Weinhold, F., NBO Version 3.1. Version 3.1.; Gaussian, Inc.: Wallingford CT, 2004.

34. (a) Kruger, H. J.; Holm, R. H. Stabilization of Trivalent Nickel in Tetragonal NiS_4N_2 and NiN_6 Environments: Synthesis, Structures, Redox Potentials and Observations Related to [NiFe]-Hydrogenases. *J. Am. Chem. Soc.* **1990,** *112*, 2955-2963; (b) Osterloh, F.; Saak, W.; Pohl, S. Unidentate and Bidentate Binding of Nickel(II) Complexes to an Fe_4S_4 Cluster via Bridging Thiolates: Synthesis, Crystal Structures, and Electrochemical Properties of Model Compounds for the Active Sites of Nickel Containing CO Dehydrogenase/Acetyl-CoA. *J. Am. Chem. Soc.* **1997,** *119*, 5648-5656; (c) O'Toole, M. G.; Kreso, M.; Kozlowski, P. M.; Mashuta, M. S.; Grapperhaus, C. A. Spin-state-dependent Oxygen Sensitivity of Iron Dithiolates: Sulfur Oxygenation or Disulfide Formation. *J. Biol. Inorg. Chem.* **2008,** *13*, 1219-1230.

35. Ohki, Y.; Tatsumi, K. Thiolate-Bridged Iron-Nickel Models for the Active Site of [NiFe] Hydrogenase. *Eur. J. Inorg. Chem.* **2011,** *2011*, 973-985.

36. Stock, A.; Azran, O.; Garden, B.; Solaimanzadeh, J.; Lo, W.; Jiang, J. Synthesis of *fac*-$[Fe^{II}(CN)(CO)_3I_2]^-$ and Chemistry of the *fac*-$[Fe^{II}(CN)_x(CO)_3I_{3-x}I]^-$ Series (x=1-3). *Inorg. Chem. Commun.* **2012,** *18*, 105-109.

37. Addison, A. W.; Rao, T. N.; Reedijk, J.; van Rijn, J.; Verschoor, G. C. Synthesis, Structure, and Spectroscopic Properties of Copper(II) Compounds Containing Nitrogen–Sulphur Donor Ligands; the Crystal and Molecular Structure of Aqua[1,7-bis(N-methylbenzimidazol-2′-yl)-2,6-dithiaheptane]copper(II) Perchlorate. *J. Chem. Soc., Dalton Trans.* **1984**, 1349-1356.

38. Slater, J. C. Atomic Radii in Crystals. *J. Chem. Phys.* **1964,** *41*, 3199-3204.

39. Rampersad, M. V.; Jeffery, S. P.; Golden, M. L.; Lee, J.; Reibenspies, J. H.; Darensbourg, D. J.; Darensbourg, M. Y. Characterization of Steric and Electronic Properties of NiN_2S_2 Complexes as S-Donor Metallodithiolate Ligands. *J. Am. Chem. Soc.* **2005,** *127*, 17323-17334.

40. Bréfuel, N.; Collet, E.; Watanabe, H.; Kojima, M.; Matsumoto, N.; Toupet, L.; Tanaka, K.; Tuchagues, J.-P. Nanoscale Self-Hosting of Molecular Spin-States in the Intermediate Phase of a Spin-Crossover Material. *Chem. Eur. J.* **2010,** *16*, 14060-14068.

41. Ma, H.; Petersen, J. L.; Young, V. G.; Yee, G. T.; Jensen, M. P. Solid-State Spin Crossover of Ni(II) in a Bioinspired N_3S_2 Ligand Field. *J. Am. Chem. Soc.* **2011,** *133*, 5644-5647.

42. Darensbourg, M. Y.; Lyon, E. J.; Smee, J. J. The Bio-organometallic Chemistry of Active Site Iron in Hydrogenases. *Coord. Chem. Rev.* **2000,** *206-207*, 533-561.

43. Fichtner, C.; Laurich, C.; Bothe, E.; Lubitz, W. Spectroelectrochemical Characterization of the [NiFe] Hydrogenase of *Desulfovibrio vulgaris* Miyazaki F. *Biochemistry* **2006,** *45*, 9706-9716.

44. Franks, M.; Gadzhieva, A.; Ghandhi, L.; Murrell, D.; Blake, A. J.; Davies, E. S.; Lewis, W.; Moro, F.; McMaster, J.; Schröder, M. Five Coordinate M(II)-Diphenolate [M = Zn(II), Ni(II), and Cu(II)] Schiff Base Complexes Exhibiting Metal- and Ligand-Based Redox Chemistry. *Inorg. Chem.* **2013,** *52*, 660-670.

45. (a) Gray, L. R.; Higgins, S. J.; Levason, W.; Webster, M. Co-ordination Chemistry of Higher Oxidation States. Part 8. Nickel(III) Complexes of Bi- and Multi-dentate Phosphorus and Arsenic Ligands; Crystal and Molecular Structure of $[Ni(Ph_2PCH_2CH_2PPh_2)Br_3]\cdot C_6H_5Me$. *J. Chem. Soc., Dalton Trans.* **1984**, 459-467; (b) Lappin, A. G.; McAuley, A., The Redox Chemistry of Nickel. In *Adv. Inorg. Chem.*, 1988; Vol. 32, pp 241-295; (c) Sacconi, L. Five Coordination in 3*d* Metal Complexes. *Pure Appl. Chem.* **1968,** *17*, 95-127.

46. Lubitz, W.; Reijerse, E.; van Gastel, M. [NiFe] and [FeFe] Hydrogenases Studied by Advanced Magnetic Resonance Techniques. *Chem. Rev.* **2007,** *107*, 4331-4365.

47. Kampa, M.; Lubitz, W.; van Gastel, M.; Neese, F. Computational Study of the Electronic Structure and Magnetic Properties of the Ni-C state in [NiFe] Hydrogenases Including the Second Coordination Sphere. *J. Biol. Inorg. Chem.* **2012,** *17*, 1269–1281.

48. Kampa, M.; Pandelia, M. E.; Lubitz, W.; van Gastel, M.; Neese, F. A Metal-Metal Bond in the Light-Induced State of [NiFe] Hydrogenases with Relevance to Hydrogen Evolution. *J. Am. Chem. Soc.* **2013,** *135*, 3915-3925.

49. Neese, F. Metal and Ligand Hyperfine Couplings in Transition Metal Complexes: The Effect of Spin–orbit Coupling as Studied by Coupled Perturbed Kohn–Sham Theory. *J. Chem. Phys.* **2003,** *118*, 3939-3948.

50. Reed, A.; Weinstock, R.; Weinhold, F. Natural Population Analysis. *J. Chem. Phys.* **1985,** *83*, 735-746.

51. (a) Ogata, H.; Mizoguchi, Y.; Mizuno, N.; Miki, K.; Adachi, S.; Yasuoka, N.; Yagi, T.; Yamauchi, O.; Hirota, S.; Higuchi, Y. Structural Studies of the Carbon Monoxide Complex of [NiFe]hydrogenase from *Desulfovibrio vulgaris* Miyazaki F: Suggestion for the Initial Activation Site for Dihydrogen. *J. Am. Chem. Soc.* **2002,** *124*, 11628-11635; (b) Pandelia, M.-E.; Ogata, H.; Currell, L. J.; Flores, M.; Lubitz, W. Inhibition of the [NiFe] Hydrogenase from *Desulfovibrio vulgaris* Miyazaki F by Carbon Monoxide : An FTIR and EPR Spectroscopic Study. *BBA - Bioenergetics* **2010,** *1797*, 304-313; (c) Stein, M.; Lubitz, W. Relativistic DFT Calculations of the Reaction Cycle Intermediates of {NFe] Hydrogenase: A Contribution to Understanding of the Enzymatic Mechanism. *J. Inorg. Biochem.* **2004,** *98*, 862-877.

52. Ohki, Y.; Ando, T.; Shimokata, S.; Tatsumi, K. A Model for the CO-inhibited Form of [NiFe] Hydrogenase: Synthesis of $(CO)_3Fe(\mu\text{–}S^tBu)_3Ni\{SC_6H_3\text{-}2,6\text{-}(mesityl)_2\}$ and Reversible CO Addition at the Ni Site. *Proc. Nat. Acad. Sci., U.S.A.* **2010,** *107*, 3994-3997.

53. (a) Matsumoto, T.; Kabe, R.; Nonaka, K.; Ando, T.; Yoon, K.-S.; Nakai, H.; Ogo, S. Model Study of CO Inhibition of [NiFe]hydrogenase. *Inorg. Chem.* **2011,** *50*, 8902-8906; (b) Sun, P.; Yang, D.; Li, Y.; Zhang, Y.; Su, L.; Wang, B.; Qu, J. Thiolate-Bridged Nickel-Iron and Nickel-Ruthenium Complexes Relevant to the CO-Inhibited State of {NiFe]-Hydrogenase. *Organometallics* **2014,** *35*, 751-757.

54. (a) Barondeau, D. P.; Kassmann, C. J.; Bruns, C. K.; Tainer, J. A.; Getzoff, E. D. Nickel Superoxide Dismutase Structure and Mechanism. *Biochemistry* **2004,** *43*, 8038-8047; (b) Fiedler, A. T.; Bryngelson, P. A.; Maroney, M. J.; Brunold, T. C. Spectroscopic and Computational Studies of Ni Superoxide Dismutase: Electronic Structure Contributions to Enzymatic Function. *J. Am. Chem. Soc.* **2005,** *127*, 5449-5462; (c) Wuerges, J.; Lee, J.-W.; Yim, Y.-I.; Yim, H.-S.; Kang, S.-O.; Djinovic Carugo, K. Crystal Structure of Nickel-containing Superoxide Dismutase Reveals Another Type of Active Site. *Proc. Nat. Acad. Sci., U.S.A.* **2004,** *101*, 8569-8574.

55. (a) Broering, E. P.; Dillon, S.; Gale, E. M.; Steiner, R. A.; Telser, J.; Brunold, T. C.; Harrop, T. C. Accessing Ni(III)-Thiolate Versus Ni(II)-Thiyl Bonding in a Family of Ni-N_2S_2 Synthetic Models of NiSOD. *Inorg. Chem.* **2015,** *54*, 3815-3828; (b) Stenson, P. A.; Board, A.; Marin-Becerra, A.; Blake, A. J.; Davies, E. S.; Wilson, C.; McMaster, J.; Schroder, M. Molecular and Electronic Structures of One-electron Oxidized Ni^{II}-(dithiosalicylidenediamine) complexes: Ni^{III}-thiolate *versus* Ni^{II}-thiyl Radical States. *Chem. Eur. J.* **2008,** *14*, 2564-2576.

56. Foerster, S.; Stein, M.; Brecht, M.; Ogata, H.; Higuchi, Y.; Lubitz, W. Single Crystal EPR studies of the Reduced Active Site of [NiFe] Hydrogenase from *Desulfovibrio vulgaris* Miyazaki F. *J. Am. Chem. Soc.* **2003,** *125*, 83-93.

For Table of Contents Only

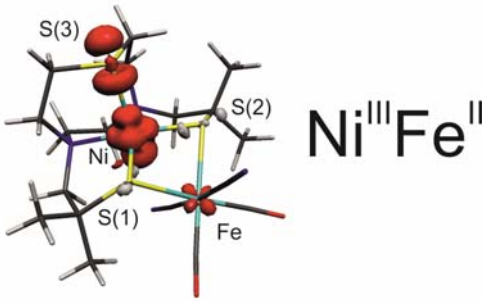

Synopsis:

Three binuclear [NiFe] complexes, incorporating {$Fe(CO)_2(CN)_2$} units, reproduce the key features of the active sites of the [NiFe] hydrogenases. [$Ni(N_2S_3)Fe(CO)_2(CN)_2$] undergoes reversible Ni-centered oxidation to form a formal $Ni^{III}Fe^{II}$ species that possesses an electronic structure that is analogous to that proposed for the Ni-C state of the [NiFe] hydrogenases.